minerals

MDPI

Article

Geochemistry of Red Soils in the Kas District of Antalya (Türkiye) Using Multivariate Statistical Approaches and GIS

Ozge Ozer Atakoglu *, Mustafa Gurhan Yalcin, Yasemin Leventeli and Bekir Taner San

Department of Geological Engineering, Akdeniz University, 07058 Antalya, Türkiye; gurhanyalcin@akdeniz.edu.tr (M.G.Y.); leventeli@akdeniz.edu.tr (Y.L.); tanersan@akdeniz.edu.tr (B.T.S.)
* Correspondence: oozer@akdeniz.edu.tr

Abstract: Red soil is formed by weathering due to the effect of bedrock and various fluids in subtropical and tropical climate zones. The major and trace element geochemistry of red soil are important for understanding its environmental conditions and interpreting its genesis. This study aims to determine how red soil is formed in the study area, where magmatic rocks are located, and to determine their relationship with magmatic fluids. In this context, geochemical analyses were conducted, and index values, spatial distributions, and multivariate statistics of the samples were calculated. Methods: A total of 49 red soil samples collected from the Sutlegen Village in the Kas district of Antalya were subjected to geochemical analysis. The following major elements were found in the red soil samples: Al_2O_3, SiO_2, Fe_2O_3, TiO_2, CaO, MgO, K_2O, P_2O_5, and SO_3. The Al_2O_3–SiO_2–Fe_2O_3 triangular diagram revealed that the samples underwent moderate laterization. Multivariate statistical analyses indicated that major element oxides of Al_2O_3, Fe_2O_3, and SiO_2 behaved differently from other components and revealed that red soil formations were associated with magmatic fluids. The region is a potential area for economic bauxite resources. Detailed investigations should be conducted on mineral exploration for bauxite ore.

Keywords: red soil; mineral exploration; geochemistry; spatial distribution; multivariate statistical analysis; Antalya; Kas

check for updates

Citation: Ozer Atakoglu, O.; Yalcin, M.G.; Leventeli, Y.; San, B.T. Geochemistry of Red Soils in the Kas District of Antalya (Türkiye) Using Multivariate Statistical Approaches and GIS. *Minerals* **2023**, *13*, 772. https://doi.org/10.3390/min13060772

Academic Editor: Maria Economou-Eliopoulos

Received: 8 May 2023
Revised: 29 May 2023
Accepted: 2 June 2023
Published: 5 June 2023

Copyright: © 2023 by the authors. Licensee MDPI, Basel, Switzerland. This article is an open access article distributed under the terms and conditions of the Creative Commons Attribution (CC BY) license (https://creativecommons.org/licenses/by/4.0/).

1. Introduction

About 15% (22 million km^2) of the continental crust of the earth consists of karstic lands [1,2]. Reddish soils with a high clay content that have been usually formed in karstic environments are called red soil. Red soil is common in Southeast Asia, Mediterranean coasts, and North America [2]. In Türkiye, red soil formations are observed in the Mediterranean, Aegean, and Marmara regions [3–6].

Several studies in the literature have examined the geochemical formations and model characterizations of red soil. The heavy metal enrichment in the red soil in western Sicily was associated with mineralogical compositions such as hematite, goethite, and magnetite [7]. Hematite and lithiophorite minerals observed in the red soil samples collected from Eastern Piedmont in the US caused the enrichment of Fe_2O_3 and MnO and their accumulation in the environment [8]. It was determined that the red soil in the Guizhou province (China) was mainly composed of SiO_2, Al_2O_3, and Fe_2O_3 [1]. The high Fe_2O_3 concentration observed in the red soil in Saudi Arabia was associated with goethite and hematite minerals [9]. The major element contents of the red soil in Jordan were found to be SiO_2, Al_2O_3, TiO_2, Fe_2O_3, and K_2O [10]. The genesis of the red soil in the Kucukkoras region in the Karaman province of Türkiye was attributed to the carbonate rocks (recrystallized limestone, cherty limestone, oolitic limestone), and the major elemental content of the red soil was found to contain Al, Ti, and Si while its trace elemental content was found to contain Ni, Mn, and Cr [4]. The major elemental content of the red soil samples from the Ibradi region in Antalya (Türkiye) was found to contain SiO_2, Al_2O_3, MgO, CaO, MnO,

and Fe_2O_3, while the trace elemental content was found to contain V, Cr, Ni, Cu, Zn, Ga, Rb, Sr, Y, Zr, Nb, Mo, Ce, and Pb [6]. It was found that the red soil of Ireland was composed of kaolinite and sepiolite minerals with rich silica content, having a lattice structure, and that their genesis was attributed to the basaltic rocks [11]. The trace elements of Cr, As, Cd, Zn, As, and Bi were found to be enriched in the red soil associated with dolomitic parent rock on the Yunnan–Guizhou Plateau [12].

The genesis of red soil formations is controversial. The studies on the genesis of red soil formations have suggested three theories. The first theory states that autochthonous red soil was formed by the weathering of the carbonated or non-carbonated rocks in the region under acidic environmental conditions [13].

The second theory states that red soil with allochthonous genesis was formed by the accumulation and weathering of the carbonate materials in the environment by different transport mechanisms (erosion, wind, flood, eolian processes) [14–16]. This type of soil has been formed by the intensive weathering process of, particularly, limestones and dolomite carbonate in subtropical and tropical climatic zones (monsoon climate zones); additionally, it is observed to have silt and clay content such as chlorite, vermiculite, and illite, and to be in colors ranging from brown to red [1–18]. The neutral pH conditions, as well as various mineral and element compositions, play an active role in these formations [14].

The third theory covers the red soil formed by undergoing metasomatic transformation processes [18–21].

The study area, Sutlegen Village, is located within the borders of the Kas district of Antalya province (Figure 1). It has a boundary with the Demre district on the east and with the Elmali district on the north. It is located approximately 30 km from the harbor of Kas. In the literature, there are several studies on the geology of the region. However, no study has been conducted on the interpretation of the genesis and chemical properties of the red soil in the region by using various methods. In this context, the present study aims to obtain the chemical properties of the red soil formed in the region. Using the results of the chemical analysis, the geostatistical analyses, the spatial distributions, and the characterization of the formation model were conducted.

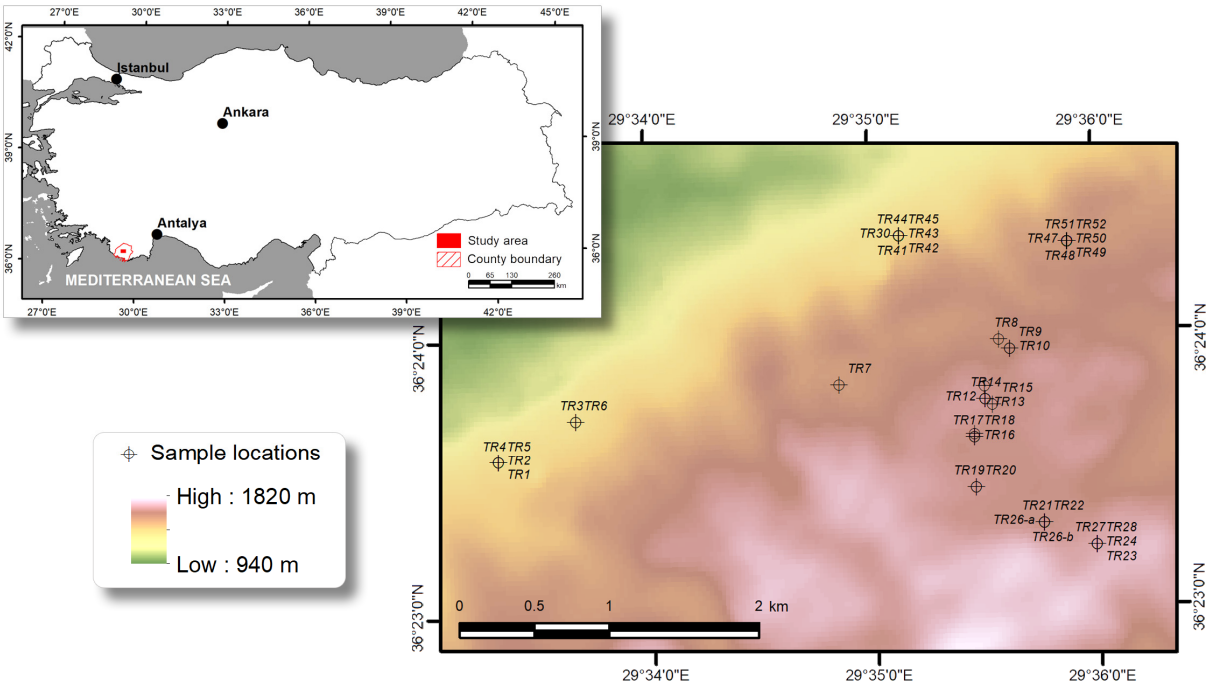


Figure 1. The location map of the study area.

2. Study Area and Regional Geology

The study area in the Sutlegen Village is located in the Kas district of Antalya province, and it is bounded by the Katran Mountain in the north and Caybogazi Dam in the northeast. The study area is covered by the geologic map sheets of FETHIYE-P 23-a1 and FETHIYE-P 23-a2 with a scale of 1/25,000, produced by the General Directorate of Mineral Research and Exploration (MTA). The lithological units observed in the study area are mostly karstifiable carbonate rocks (Figure 2) [22]. The lithological and stratigraphic characteristics of these rocks are as follows: (1) Beydaglari Formation (Kb): the formation, which is predominant in the study area, consists of karstifiable Liassic-Upper Cretaceous aged neritic limestones. (2) Gomuce Member (Tmsg): the unit, which consists of Burdigalian aged limestones, forms the bottom border of the Sinekci Formation. (3) Kibrisdere Member (Tmsk): the unit, which consists of Burdigalian aged clayey limestones, has fossil content. (4) Felenkdagi Conglomerate (Tmf): the unit, which was found to be Upper Langhian-Serravalian (?) aged, consists of gravel and conglomerates of various sizes and shapes. The unit also includes sandy limestone, sandstone, and mudstone. (5) Kasaba Formation (Tmka): the formation, which consists of different sedimentary intercalations of Upper Burdigalian-Lower Langhian aged units, consists of sandstone, conglomerate, claystone, and siltstone [22]. (6) Caybogazi Member (Tmsc): the unit, which is covered by the Sinekci formation, is characterized by the Burdigalian aged clay stones. (7) Susuzdag Formation (Tes): the unit, which was found to be Upper Lutetian-Priabonian aged, consists of limestones and recrystallized limestones with nummulite fossil content [22]. The units that have the latest formation in the study area and that are not suitable for karstification are Quaternary-aged alluvium (Qal) and slope debris (Qym) [23].

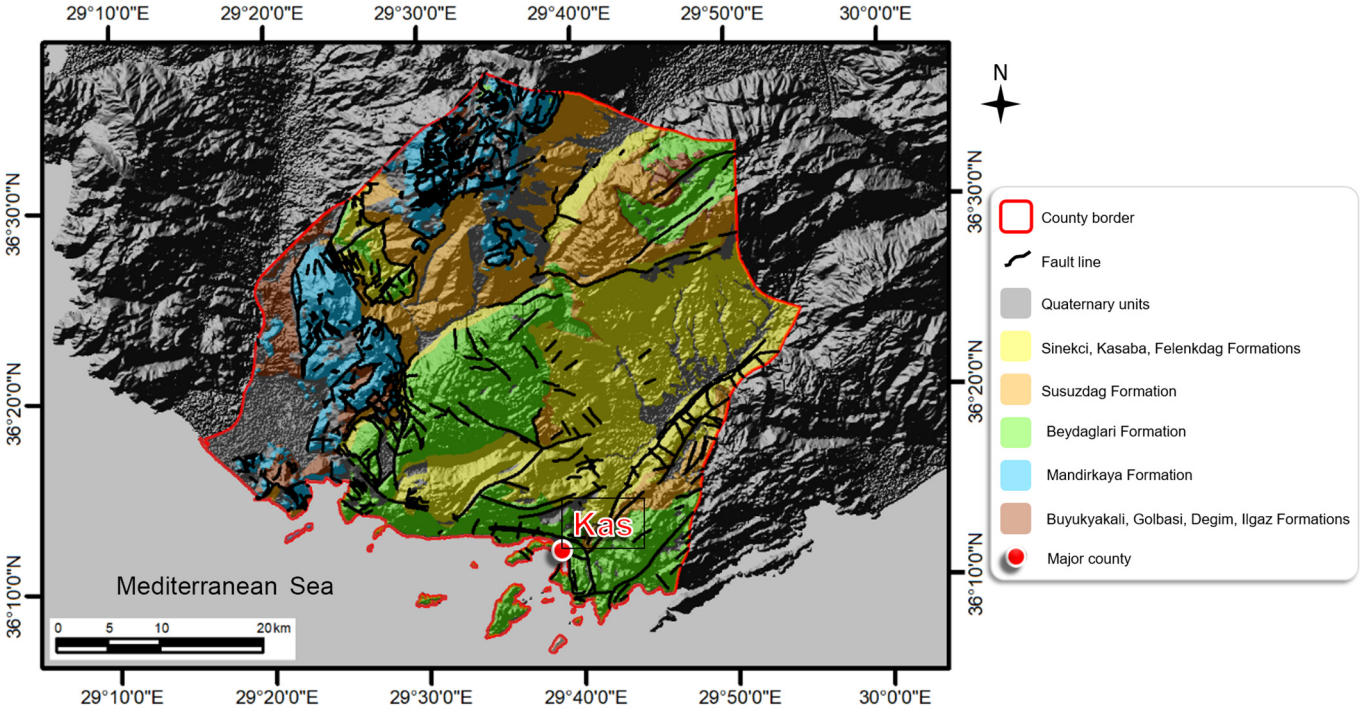


Figure 2. Regional geologic map of the study area (modified after in [22,23]).

3. Analytical Methods

3.1. Geochemical Analyses

The red soils formed due to the bauxite deposit in the study area are located close to the surface. The selected samples were collected from the surface outcrop considering the regional geology of the study area. A total of 49 red soil samples related to magmatic fluids were collected from the Sutlegen Village, which is located in the Kas district of

Antalya province (Türkiye). The collected samples were analyzed by the Mineral Deposits Laboratory in the Department of Geological Engineering at the Faculty of Engineering of Akdeniz University. The samples, which were taken out of plastic bags, were homogenized and ground to a size of <10 µm using the RM 200 mortar grinder (Retsch GmbH, Germany). Then, press-pastilles were produced using the press machine under a pressure of 30 MPa to have suitable dimensions, sizes, and smooth surfaces for the X-ray fluorescence spectrometry analysis [24].

The major oxide elements (in %) (Fe_2O_3, MgO, Al_2O_3, CaO, SiO_2, TiO_2, K_2O, P_2O_5, and SO_3), the trace elements (in ppm) (Cr, Zn, Mn, V, Co, Sr, Ni, Cu, Ce, Y, La, Nb, Cl, Ba, Pb, As, U, Th, Ga, Hf, Sn, Rb, W, Au, Pt, Te, Br, Sb, Ta, Hg, and Cd), and some rare earth elements in the red soil samples were measured with ppm precision by using a Rigaku NEX CG Energy Dispersive X-Ray Fluorescence (ED-XRF) spectrometer (NEX-CG Applied Rigaku Technologies, Inc. Austin, TX, USA) (Table 1).

3.2. Statistical Analyses

The obtained results were evaluated using the analytical method. The rare earth, trace, and major oxide element concentrations were assessed and interpreted using multivariate statistical methods. The following multivariate statistical analyses were considered appropriate for the study: correlation analysis, simple linear regression, factor analysis, and cluster analysis. The SPSS 23 statistical software was used to obtain these statistics.

3.3. Paleoclimatic Characteristics of the Red Soil Samples

The red soil formations present information on paleoenvironmental and paleoclimatic changes [2,12,25]. In this context, index values calculated using the results of the geochemical analysis of the red soil samples are significant for the interpretation of the formation processes and examining the genesis. Therefore, numerous indices were computed. During the study, the Chemical Index of Alteration (CIA), Chemical Index of Weathering (CIW), Plagioclase Index of Alteration (PIA), and Silica to Alumina Ratio/Ruxton Ratio (R) were computed.

In order to understand the physical and chemical weathering conditions of the red soil that has been formed through the formation processes, the chemical index of alteration (CIA) is computed. The cations of Na^+, K^{2+}, and Ca^{2+} in minerals such as feldspar, which is an important part of the weathering processes, tend to diminish in the environment [26,27]. The CIA index is calculated using the values of the major element oxides of Al_2O_3, Na_2O, K_2O, and CaO (Equations (1) and (2)) to understand the chemical weathering processes [28].

$$\mathrm{CIA} = \left[\frac{\mathrm{Al_2O_3}}{(\mathrm{Al_2O_3} + \mathrm{Na_2O} + \mathrm{K_2O} + \mathrm{CaO})}\right] \times 100 \quad (1)$$

$$\mathrm{CaO*} = \mathrm{ml\ CaO} - \left[\left(\frac{10}{3}\right) \times \mathrm{mol\ P_2O_5}\right] \quad (2)$$

Equations (3) and (4) are used to compute the chemical index of weathering (CIW) of the red soil samples to obtain information about weathering processes and the paleoclimatic behavior of the environment [29].

$$\mathrm{CIW} = \left[\frac{\mathrm{Al_2O_3}}{(\mathrm{Al_2O_3} + \mathrm{CaO*} + \mathrm{Na_2O})}\right] \times 100 \quad (3)$$

$$\mathrm{CaO*} = \mathrm{ml\ CaO} - \left[\left(\frac{10}{3}\right) \times \mathrm{mol\ P_2O_5}\right] \quad (4)$$

Table 1. Geochemical analyses results of red soil samples (the major oxide elements (in %); trace elements and some rare earth elements (in ppm).

Sample Code	Latitude	Longitude	Al_2O_3	SiO_2	Fe_2O_3	TiO_2	CaO	MgO	P_2O_5	SO_3	Mn	Cr	V	Co	Sr	Ni	Zn	Ce	Y	La	Cu	Nb	Ba
TR1	36.3927778	29.5552778	44.8	34.7	16.4	1.94	0.399	0.550	0.140	0.01	496	347	646	436	130	414	296	158	98.7	72.8	104	102	ND
TR2	36.3927778	29.5552778	38.0	40.9	15.4	2.18	0.791	1.140	0.181	0.09	636	352	501	424	169	352	280	170	118	127	84.6	82.6	172
TR3	36.3951083	29.5611111	40.4	38.2	16.4	2.06	0.605	0.857	0.181	0.07	579	366	628	397	297	390	257	ND	102	ND	90.8	81.6	113
TR4	36.5591333	29.5627722	50.8	28.5	16.9	2.14	0.300	0.382	0.151	0.03	536	391	781	441	124	ND	257	169	146	ND	113	108	46.6
TR5	36.5591333	29.5627722	42.0	35.9	16.4	2.37	0.650	0.908	0.257	0.12	102	541	595	468	293	472	343	194	188	243	122	105	147
TR6	36.5591333	29.5627722	42.5	35.3	16.6	2.41	0.622	0.893	0.266	0.11	975	512	611	456	268	465	358	197	203	265	91.7	116	129
TR7	36.3969528	29.5808333	38.0	43.3	11.5	1.92	3.170	1.150	0.220	0.13	730	368	188	325	309	337	295	ND	147	91.5	125	89.7	166
TR8	36.3994583	29.5927778	44.1	34.9	16.0	2.47	0.451	0.553	0.229	0.07	159	407	526	398	393	363	319	216	167	133	153	101	119
TR9	36.3988917	29.5936111	45.4	33.5	16.4	2.44	0.323	0.485	0.217	0.05	176	483	595	427	384	383	333	155	172	ND	152	116	ND
TR10	36.3988917	29.5936111	44.8	34.5	15.7	2.68	0.366	0.544	0.199	0.06	838	491	469	386	267	274	344	199	112	116	115	101	110
TR11	36.3966833	29.5916667	43.5	34.2	17.1	2.95	0.340	0.515	0.226	0.05	832	447	602	408	297	295	367	243	120	135	115	113	115
TR12	36.3958972	29.5916667	47.6	32.6	15.5	2.25	0.345	0.491	0.227	0.06	541	492	376	361	286	301	226	201	91.7	133	120	97.5	104
TR13	36.3958972	29.5916667	47.1	31.2	17.0	2.50	0.348	0.545	0.225	0.06	694	484	478	393	266	319	248	222	92.6	142	111	108	110
TR14	36.3958972	29.5916667	46.0	31.1	18.0	2.80	0.281	0.483	0.209	0.04	747	466	475	398	264	341	321	241	93.3	151	122	98.0	130
TR15	36.3955639	29.5922222	45.8	34.6	14.6	2.51	0.446	0.505	0.291	0.13	159	521	463	470	533	349	357	179	194	129	129	94.1	114
TR16	36.3938194	29.5908333	52.0	24.7	18.9	2.57	0.260	0.443	0.195	0.06	704	616	426	463	255	316	296	249	108	170	113	109	98.9
TR17	36.3936111	29.5908333	45.7	30.8	17.9	2.86	0.813	0.552	0.212	0.06	103	592	ND	380	274	331	313	230	100	129	121	106	138
TR18	36.3936111	29.5908333	47.4	25.4	19.9	3.57	1.990	0.500	0.284	0.08	100	873	ND	466	478	358	281	338	112	169	97.3	110	103
TR19	36.3905556	29.5908333	44.6	30.3	19.2	3.52	0.328	0.687	0.343	0.11	963	738	ND	438	470	362	269	311	110	152	85.7	130	119
TR20	36.3905556	29.5908333	53.8	20.8	21.2	2.91	0.231	ND	0.253	0.06	863	654	987	534	366	364	266	261	115	ND	99.3	128	ND
TR21	36.3883333	29.5958333	37.4	37.3	15.8	2.32	4.390	0.956	0.327	0.17	163	545	502	392	445	249	255	208	127	138	110	88.7	166
TR22	36.3883333	29.5958333	44.6	33.9	16.3	2.52	0.664	0.572	0.309	0.14	912	676	441	400	411	290	270	240	119	185	117	97.2	127
TR23	36.38695	29.5997222	47.6	29.3	18.6	2.39	0.387	0.543	0.241	0.09	935	576	654	505	346	418	296	209	191	135	126	126	ND
TR24	36.38695	29.5997222	51.3	23.7	20.4	3.17	0.328	ND	0.327	0.07	734	822	230	493	454	223	242	331	105	224	96.2	140	116
TR25	36.4058333	29.5855556	49.8	24.6	20.0	3.39	0.654	0.337	0.343	0.09	982	812	80.9	450	510	250	258	365	119	256	96.9	144	119
TR26-a	36.3883333	29.5958333	48.6	26.2	19.4	3.22	0.648	0.465	0.407	0.12	113	892	436	490	657	271	266	283	128	217	85.2	135	127
TR26-b	36.3883333	29.5958333	51.2	22.7	20.8	2.91	0.494	0.371	0.353	0.11	179	715	716	529	503	371	374	272	181	170	114	130	ND
TR27	36.3869500	29.5997222	49.6	24.3	19.8	3.35	1.030	0.402	0.480	0.12	125	868	297	471	878	294	312	307	167	224	109	144	142
TR28	36.3869500	29.5997222	49.8	27.4	18.5	3.11	0.201	ND	0.233	0.05	599	816	ND	407	353	261	227	288	89.3	170	86.8	106	102
TR29	36.4058333	29.5855556	42.1	31.3	21.4	2.52	0.317	0.591	0.372	0.07	373	593	ND	471	451	336	396	215	129	98.1	135	80.8	284
TR30	36.4058333	29.5855556	41.0	32.9	21.0	2.50	0.360	0.519	0.348	0.08	746	521	703	434	556	314	316	165	168	ND	135	89.6	87.2
TR32	36.4052778	29.5980556	46.7	34.8	13.8	2.59	0.328	0.423	0.347	0.10	104	505	ND	387	992	352	267	179	295	132	268	105	109
TR33	36.4052778	29.5980556	47.3	35.7	12.1	2.74	0.338	0.441	0.372	0.09	496	521	363	303	114	335	259	213	314	150	216	127	125
TR34	36.4052778	29.5980556	46.9	28.4	20.2	2.58	0.258	0.434	0.338	0.08	100	685	433	445	517	309	306	247	160	162	102	115	121
TR37	36.4052778	29.5980556	45.0	30.9	18.7	3.00	0.174	0.586	0.379	0.10	155	696	ND	438	546	275	309	252	151	174	130	116	138
TR38	36.4052778	29.5980556	43.3	34.1	17.8	2.38	0.371	0.629	0.064	0.11	731	582	625	394	370	281	235	219	86.5	ND	84	83.7	103
TR39	36.4052778	29.5980556	44.5	33.5	17.2	2.34	0.396	0.621	0.368	0.10	833	557	713	372	337	284	245	168	88.7	ND	100	110	87.2
TR40	36.4052778	29.5980556	33.0	46.9	13.2	2.71	1.050	1.550	0.027	0.19	144	335	ND	322	184	204	211	109	91.8	ND	81.8	65.9	278

Table 1. *Cont.*

Sample Code	Latitude	Longitude	Al_2O_3	SiO_2	Fe_2O_3	TiO_2	CaO	MgO	P_2O_5	SO_3	Mn	Cr	V	Co	Sr	Ni	Zn	Ce	Y	La	Cu	Nb	Ba
TR41	36.4058333	29.5855556	43.8	33.6	17.6	2.29	0.463	0.677	0.266	0.11	137	542	691	485	223	315	292	211	106	126	119	113	ND
TR42	36.4058333	29.5855556	51.7	30.9	13.3	2.77	0.178	ND	0.310	0.10	479	591	ND	424	982	431	330	195	358	117	127	130	ND
TR43	36.4058333	29.5855556	49.1	29.0	17.6	2.44	0.238	0.333	0.316	0.08	784	465	595	461	830	386	330	204	343	147	125	118	ND
TR44	36.4058333	29.5855556	52.1	24.1	19.8	2.46	0.263	0.348	0.168	0.05	449	559	866	474	205	310	198	208	81.1	ND	89.9	105	ND
TR45	36.4058333	29.5855556	41.3	43.5	11.0	2.29	0.335	0.441	0.195	0.04	103	439	290	281	414	279	272	151	167	103	111	87.2	134
TR46	36.4052778	29.5980556	52.4	23.7	18.8	3.28	0.318	0.353	0.245	0.07	916	694	ND	404	306	490	355	317	137	194	145	122	121
TR47	36.4052778	29.5980556	45.1	29.9	18.3	2.93	1.000	0.795	0.337	0.22	152	633	601	485	407	380	335	291	154	173	191	133	154
TR48	36.4052778	29.5980556	50.1	24.7	19.6	3.14	0.399	0.508	0.312	0.10	122	686	691	429	450	37.7	358	307	172	221	166	142	110
TR49	36.4052778	29.5980556	49.8	25.5	19.6	2.86	0.412	0.495	0.270	0.09	193	690	467	467	323	287	340	270	171	176	117	126	130
TR50	36.4052778	29.5980556	51.9	24.4	19.3	2.63	0.227	0.360	0.176	0.04	126	649	893	504	200	370	265	275	139	130	120	123	ND
TR52	36.4052778	29.5980556	52.1	23.6	20.1	2.67	0.414	ND	0.156	0.04	116	648	900	484	189	346	267	255	123	133	118	127	ND

Sample Code	Pb	Cl	As	Th	Ga	Hf	Sn	Rb	W	U	La	Au	Pt	Br	Sb	Hg	Cd	Te	Tl	Bi	Ir	In	Se	Ge
TR1	84	89.6	59.2	46.2	55.9	22.9	40.3	39.5	18.0	6.5	72.8	6.6	7.6	8.1	17.8	8.2	6.1	ND	ND	4	ND	ND	ND	ND
TR2	71.4	103	73.1	40.3	48.3	28.8	38.0	70.9	18.9	5.8	127	6.6	10.2	18.7	17.0	ND	6.1	ND	ND	ND	ND	ND	ND	ND
TR3	72.6	90.4	65.9	38.7	48.6	23.1	35.1	53.5	26.2	7.0	ND	ND	10.8	12.9	ND	ND	ND	ND	ND	ND	ND	ND	ND	ND
TR4	92.5	74.9	68.7	46.9	60.2	29.6	45.0	18.9	19.4	5.9	ND	8.4	11.0	7.9	21.7	ND	4.8	ND	ND	4.8	ND	8	ND	ND
TR5	84.5	88.6	65.0	48.0	51.4	27.2	44.4	45.4	28.3	4.8	243	7.2	ND	13.4	ND	ND	ND	ND	6.9	ND	11.9	ND	ND	ND
TR6	92.2	113	70.3	49.0	48.9	46.1	33.9	36.9	ND	8.1	265	9.4	6.7	10.1	ND	7.1	ND	14.6	ND	ND	ND	ND	ND	ND
TR7	62.1	154	60.1	38.1	53.6	22.0	32.1	67.6	20.1	ND	91.5	ND	ND	23.7	ND	ND	ND	ND	4.5	ND	ND	ND	ND	ND
TR8	86.8	80.7	66.4	47.1	55.6	29.5	37.5	42.5	19.0	7.4	133	8.6	10.5	14.7	ND	ND	8.2	ND	ND	3.6	ND	ND	ND	ND
TR9	85.6	70.0	69.2	44.8	55.3	27.2	34.1	41.2	ND	5.2	ND	11.6	11.8	7.9	ND	6.8	ND	ND	ND	4.1	ND	ND	ND	ND
TR10	93.4	91.1	43.0	47.3	53.9	36.5	41.3	41.8	18.4	7.6	116	9.8	13.3	8.6	ND	ND	ND	10.5	5.1	ND	ND	ND	ND	ND
TR11	101	82.9	41.2	48.2	58.0	37.6	32.6	46.7	18.4	7.4	135	10.1	10.5	6	ND	7.8	ND	ND	ND	ND	ND	ND	ND	ND
TR12	72.7	77.7	41.9	42.5	62.7	32.1	38.0	37.8	ND	8.1	133	8.6	ND	6.7	ND	ND	12.3	11.2	3.6	ND	ND	ND	ND	ND
TR13	87.6	71	46.3	48.1	56.9	36.9	36.9	40.4	14.7	6.7	142	9	7.5	6.1	ND	ND	5.7	ND	4.9	ND	ND	ND	ND	ND
TR14	92.8	68.2	51.1	49.5	57.9	32.5	35.5	55.4	ND	7.1	151	13.8	11.2	4.4	ND	ND	5.9	ND	6.5	ND	ND	ND	ND	ND
TR15	83.7	60.8	71.3	47.3	53.9	32.0	29.6	33.9	21.6	11.9	129	5.9	ND	10	16.0	ND	15.5	ND	5.8	ND	ND	ND	ND	ND
TR16	83.0	78.5	62.9	51.4	58.9	26.2	40.5	32.7	15.7	10.2	170	9.6	10.2	6.8	ND	ND	ND	ND	5.1	ND	ND	ND	ND	ND
TR17	81.9	69.4	62.1	47.6	61.8	30.9	44.1	47.2	17.9	10	129	7.6	9.6	4.8	ND	ND	6.2	ND	6.8	4.9	ND	7	3	ND
TR18	107	68.3	104	65.8	59.0	39.6	37.2	13.2	ND	15.6	169	15.1	16.8	4.6	16.1	12.0	ND	ND	ND	ND	ND	ND	ND	ND
TR19	101	73.4	87.9	63.9	42.2	47.0	36.0	22.3	ND	14.4	152	12.6	ND	ND	ND	ND	ND	11.7	9.3	ND	14.4	ND	ND	ND
TR20	103	79.2	112	67.9	68.2	32.0	50.6	8.32	22.2	15.4	ND	9.3	ND	ND	26.9	11.3	ND	26.3	ND	ND	ND	11.3	ND	ND
TR21	81.8	79.6	53.5	ND	50.2	30.5	35.9	42.3	20.7	9.6	138	ND	11.8	22.2	ND	ND	11.4	ND	ND	ND	ND	ND	ND	ND
TR22	98.6	81.7	47.5	52.9	61.6	26.3	37.5	26.2	ND	11.0	185	10.9	ND	7.2	ND	7.2	8.6	9.33	ND	ND	ND	ND	ND	ND
TR23	100	78.1	88.6	56.4	60.2	37.2	44.9	21.0	18.0	12.5	135	8.7	ND	5.5	20.6	7.9	6.9	ND	ND	ND	ND	ND	ND	ND
TR24	116	70.5	58.7	64.6	67.4	36.9	42.3	11.5	14.4	18.2	224	12.1	11	ND	ND	ND	ND	ND	6.3	6.4	ND	ND	ND	ND
TR25	119	93.3	54.9	64.2	71.4	45.2	45.2	14.2	20	19.1	256	9.2	ND	ND	ND	11.1	ND	ND	ND	ND	ND	ND	ND	ND

Table 1. *Cont.*

Sample Code	Pb	Cl	As	Th	Ga	Hf	Sn	Rb	W	U	La	Au	Pt	Br	Sb	Hg	Cd	Te	Tl	Bi	Ir	In	Se	Ge
TR26-a	129	109	41	62	ND	63	ND	15.4	15.7	16.7	217	9.8	18.4	5	ND	9.3	ND	ND	ND	ND	ND	ND	ND	ND
TR26-b	115	86.3	88.1	67.2	56.8	76.4	48.5	16.6	ND	20	170	12.5	ND	ND	19.7	12.4	ND	ND	ND	ND	ND	ND	4.9	ND
TR27	121	84.5	48.2	70.6	66.7	41.8	45.6	17.0	ND	17.1	224	13.2	13.5	5.6	9	ND	ND	ND	ND	ND	ND	ND	ND	ND
TR28	104	69.1	54.2	64.3	58.6	30.5	42.3	13.5	17.9	12.7	170	8.3	11.8	3.5	ND	9.9	ND	ND	ND	ND	ND	ND	ND	ND
TR29	75.1	63	69.9	46.9	51.5	33.3	37.9	36.9	ND	14.5	98.1	13.2	10	ND	15.5	ND	14.7	ND	5.6	ND	ND	ND	ND	ND
TR30	84	68.2	75.1	49.8	54.7	25.1	42.6	22.8	21.1	12.8	ND	6.4	ND	ND	23	9.6	19.9	ND	ND	4.1	ND	8.6	3.9	ND
TR32	82.8	60	56.6	48.8	44.1	34.6	34.5	25.8	ND	11.6	132	7.6	ND	10.9	ND	ND	14.4	ND	4.6	ND	12.3	ND	ND	ND
TR33	88.3	57.5	45.6	52.9	49.4	52.6	37.3	32.3	24.4	9.6	150	ND	ND	9.2	7.4	8.4	ND	10.5	ND	ND	ND	ND	ND	ND
TR34	97.7	63.6	78.2	57.3	55.9	42.4	39.5	18.4	ND	14.3	162	14	10.5	ND	18.2	9.1	ND	ND	ND	ND	ND	ND	ND	ND
TR37	94.6	68.2	57.3	58	59	28.1	40.6	31.0	18.4	9.7	174	8.6	13	5.5	ND	ND	ND	ND	6	ND	ND	ND	ND	ND
TR38	84.8	69	69	52.8	52.5	38.3	44.8	26.5	ND	11.5	ND	9.3	ND	5.2	ND	ND	ND	ND	5.1	ND	ND	ND	ND	4.2
TR39	90.6	56.4	58.2	50.9	62.4	25.6	47.3	26.4	15.7	9.5	ND	9.2	8.9	ND	17	10.4	ND	ND	ND	ND	ND	ND	ND	ND
TR40	59.6	93.6	50.9	32.9	40.8	20	33.9	92.3	11.5	ND	ND	7.7	12.9	33	ND	ND	5.8	ND	ND	ND	ND	ND	ND	ND
TR41	101	67.8	68.1	54	6.4	29.1	40	32.6	19.6	9.7	126	8.3	8.3	13.7	ND	10.3	ND	ND	ND	ND	ND	ND	ND	ND
TR42	97	50.9	76.8	48	61.6	29.5	41.2	21.3	21.1	9.8	117	5.6	7.3	5.7	ND	ND	4.7	15.2	ND	3.7	ND	ND	ND	ND
TR43	96.8	86.4	93.4	48.4	56.3	37.6	41.9	22.4	24.1	8.7	147	6.4	10.4	ND	ND	ND	ND	ND	ND	ND	ND	ND	ND	5.9
TR44	90.8	79.2	79.6	50.1	64.9	30.9	39.4	15.3	217	12.9	ND	ND	ND	19	14.3	ND	ND	ND	ND	4.1	ND	ND	ND	ND
TR45	74	56.6	83.5	39	37.1	253	28.7	23.3	18.1	7.4	103	6	9.9	ND	ND	8.2	56.2	ND	ND	ND	ND	ND	ND	ND
TR46	113	63	74.6	53.7	63.2	45	49.6	22.4	20.6	13	194	7.5	ND	ND	ND	10.2	ND	19.7	ND	8.4	ND	ND	4.5	ND
TR47	117	89.9	80	60.9	57.1	40.4	46.5	40.3	19	11.2	173	9.9	11.7	8.6	15.7	ND	ND	ND	6.9	ND	ND	ND	ND	ND
TR48	133	69.9	106	65.5	59.4	50.7	44.3	37.7	ND	12.5	221	13.8	14.7	ND	ND	10.4	ND	ND	ND	ND	ND	ND	ND	ND
TR49	96.1	70.4	72.2	52.4	68.3	32.9	48.3	23.5	14.2	17.7	176	10.8	14.1	ND	18.5	ND	ND	22.1	5.2	6.8	ND	ND	ND	ND
TR50	108	65	89.3	57.6	62.9	40.9	51.5	16.3	16.8	11.2	130	10.6	10.5	ND	17.3	10.3	ND	16	ND	ND	ND	ND	ND	ND
TR52	112	67.6	81.6	69	67.5	33.6	47	14.0	ND	16.5	133	12.4	7.8	ND	ND	11.5	ND	ND	ND	ND	ND	ND	4.1	ND

ND = Not detected.

The plagioclase index of alteration (PIA) provides information about the mineral phases in the red soil samples, the source rock that played a role in the formation, and the paleoclimatic characteristics of the environment. The red soil is formed in clayey environments, where chemical weathering is at the highest levels, in the subtropical and tropical climatic zones (monsoon climate zones). The PIA index, which is computed for the environmental conditions of the clay, provides information about the extent to which the plagioclase mineral turns into clay minerals [26,30] (Equation (5)) [26].

$$\mathrm{PIA} = 100 \times \frac{(\mathrm{Al_2O_3} - \mathrm{K_2O})}{(\mathrm{Al_2O_3} + \mathrm{CaO} + \mathrm{Na_2O} - \mathrm{K_2O})}$$

$$\mathrm{Na_2Al_2Si_2O_8} + 3\mathrm{H_2O} \rightarrow \mathrm{Al_2Si_2O_5(OH)_4} + 2\mathrm{NaOH} \quad (5)$$

PlagioclaseKaolinite

The silica to alumina ratio/Ruxton ratio (R) presents information about the correlation of silica, which is one of the elemental compositions that is important in chemical weathering processes, with other elemental contents [31]. The silica ratio, which decreases in chemical weathering processes, changes in direct proportion to the Ruxton ratio. The Ruxton ratio is expected to be >10 in rocks that have not undergone chemical weathering processes [30] (Equation (6)) [31].

$$\mathrm{R} = \frac{\mathrm{SiO_2}}{\mathrm{Al_2O_3}} \quad (6)$$

3.4. Spatial Statistics

In the study, the locations of all collected samples were recorded using a Global Navigation Satellite System (Garmin Montana 680). The coordinates of all samples were collected in geographical coordinates (latitude and longitude) in the WGS84 datum. Then, all recorded samples and their corresponding measurements were combined into a dataset to obtain the spatial distribution of the samples. Next, this dataset was converted to vector points using ArcGIS 9 software. Finally, the spatial distribution of all samples and their corresponding measurements and computations were mapped using the Kriging interpolation method. In this process, the ordinary Kriging method with a spherical semivariogram model was used to generate the spatial distribution of collected samples [32]. The distribution maps of the compounds of Al_2O_3, SiO_2, Fe_2O_3, TiO_2, CaO, MgO, and K_2O, and elements of Mn and Rb, as well as the weathering indices of CIA, CIW, and PIA, were generated in raster format using the CoKriging interpolation method [33]. In CoKriging interpolation, simple and prediction methods were used to generate the spatial distribution of multiple input data sets.

4. Results

The laterization, which plays an active role in the formation of red soil, begins with the depletion of the aluminosilicate minerals and alkaline group elements in the environment under low pH conditions [34–36]. The degree of laterization reactions taking place under superficial conditions was determined by plotting the triangular diagram (modified after [37]), using the major elements of Al_2O_3, SiO_2, and Fe_2O_3 (Figure 3).

The triangular diagram of Al_2O_3–SiO_2–Fe_2O_3 was plotted to determine the degree of laterization of the red soil samples. Sample 30 and Sample 40 were found to have undergone a poor laterization, and Sample 19, Sample 20, and Sample 37 were found to have undergone a strong laterization, while all other red soil samples were found to have undergone moderate laterization. While Sample 30 and Sample 40 were found to have the lowest Al_2O_3 concentration (45,000 ppm and 328,000 ppm), Sample 20 had the highest Al_2O_3 concentration (538,000 ppm). In this context, a strong correlation was found between the degree of laterization and the Al_2O_3 concentration. The heat map revealed that the increase in the degree of laterization in the region led to Al_2O_3, TiO_2, and CaO enrichment, and SiO_2 and P_2O_5 depletion in the environment.

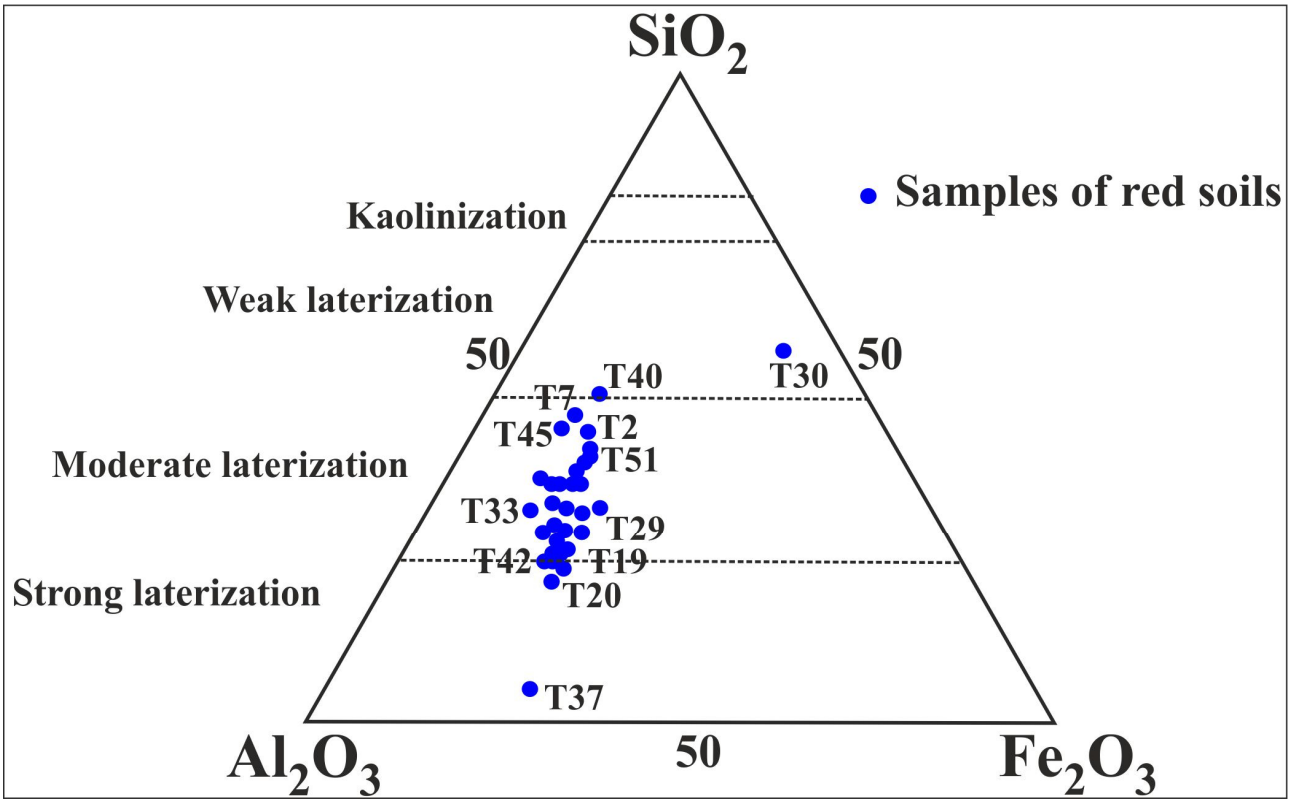


Figure 3. Triangular diagram based on [37] showing the Al_2O_3–SiO_2–Fe_2O_3 laterization degree of the study area.

Table 1 presents the coordinates, which were prepared in a format suitable for the software running the geographical information system tools, the codes of the samples, and the results of the elemental analysis in ppm. Table 2 presents the chemical alteration index values of the red soil samples.

Table 2. The chemical alteration index values of the red soil samples.

Sample Code	CIA	CIW	PIA	R
TR1	99.19	100.15	2.62	0.77
TR2	97.04	99.51	5.36	1.08
TR3	98.37	100.00	4.04	0.95
TR4	100.00	100.00	1.86	0.56
TR5	98.85	100.00	4.30	0.85
TR6	99.19	100.00	4.17	0.83
TR7	91.71	93.85	11.44	1.16
TR8	99.58	100.00	2.78	0.79
TR9	99.94	100.00	2.25	0.74
TR10	99.55	100.00	2.54	0.77
TR11	99.74	100.00	2.40	0.79
TR12	100.00	100.00	2.31	0.68
TR13	100.00	100.00	2.47	0.66
TR14	99.68	100.00	2.16	0.68
TR15	100.00	100.00	2.60	0.76
TR16	100.00	100.00	1.94	0.48
TR17	98.70	99.77	3.70	0.67
TR18	97.46	97.85	6.49	0.54
TR19	100.00	100.00	2.80	0.68

Table 2. *Cont.*

Sample Code	CIA	CIW	PIA	R
TR20	100.00	100.00	0.61	0.39
TR21	90.30	91.89	13.97	1.00
TR22	100.00	100.00	3.34	0.76
TR23	100.00	100.00	2.54	0.62
TR24	100.00	100.00	0.86	0.46
TR25	100.00	100.00	2.62	0.49
TR26-a	100.00	100.00	2.98	0.54
TR26-b	100.00	100.00	2.32	0.44
TR27	100.00	100.00	3.77	0.49
TR28	100.00	100.00	0.53	0.55
TR29	100.00	100.00	2.51	0.74
TR30	100.00	100.00	2.41	7.31
TR32	100.00	100.00	2.06	0.75
TR33	100.00	100.00	2.14	0.75
TR34	100.00	100.00	1.90	0.61
TR37	100.00	100.00	2.15	0.07
TR38	98.80	99.64	2.76	0.79
TR39	100.00	100.00	2.79	0.75
TR40	93.13	97.16	7.25	1.43
TR41	99.85	100.00	3.15	0.77
TR42	100.00	100.00	0.49	0.60
TR43	100.00	100.00	1.56	0.59
TR44	100.00	100.00	1.66	0.46
TR45	100.00	100.00	2.11	1.05
TR46	100.00	100.00	1.83	0.45
TR47	98.90	100.00	4.87	0.66
TR48	100.00	100.00	2.49	0.49
TR49	100.00	100.00	2.47	0.51
TR50	100.00	100.00	1.60	0.47
TR52	99.94	100.00	1.08	0.45

4.1. Distribution Maps

The distribution maps of some major element oxides (Al_2O_3, SiO_2, Fe_2O_3, TiO_2, CaO, MgO, and K_2O), trace elements (Mn, Rb), and indices (CIA, CIW, PIA), which were generated using the spatial analyst tool of ArcMap 9 software (ESRI 2011, ArcGIS Desktop, Release 9, Redlands, CA, Environmental Systems Research Institute, USA) package after making interpolations, are presented in Figures 4–6, respectively [38].

The results of spatial distribution were acquired from the Kriging interpolation technique utilizing the coordinates of the chemical analysis, their measurements, and computed indices: (1) K_2O and MgO have a strong positive correlation (0.922 **). (2) The plagioclase change index (PIA) and CaO also have a strong positive correlation (0.946 **). (3) There is also a strong positive correlation between the chemical change index (CIA) and the chemical index of weathering (CIW), with a correlation coefficient of 0.924**. (4) There is also a strong correlation CIW between U, K_2O, Rb, Fe_2O_3, Nb, and Cr with the value of the correlation coefficient as (−0.723 **, −0.789 **, 0.744 **, 0.732 **, 0.721 **, 0.830 **, respectively. (5) R (Ruxton ratio) and Al_2O_3 have a strong negative correlation (−0.888 **).

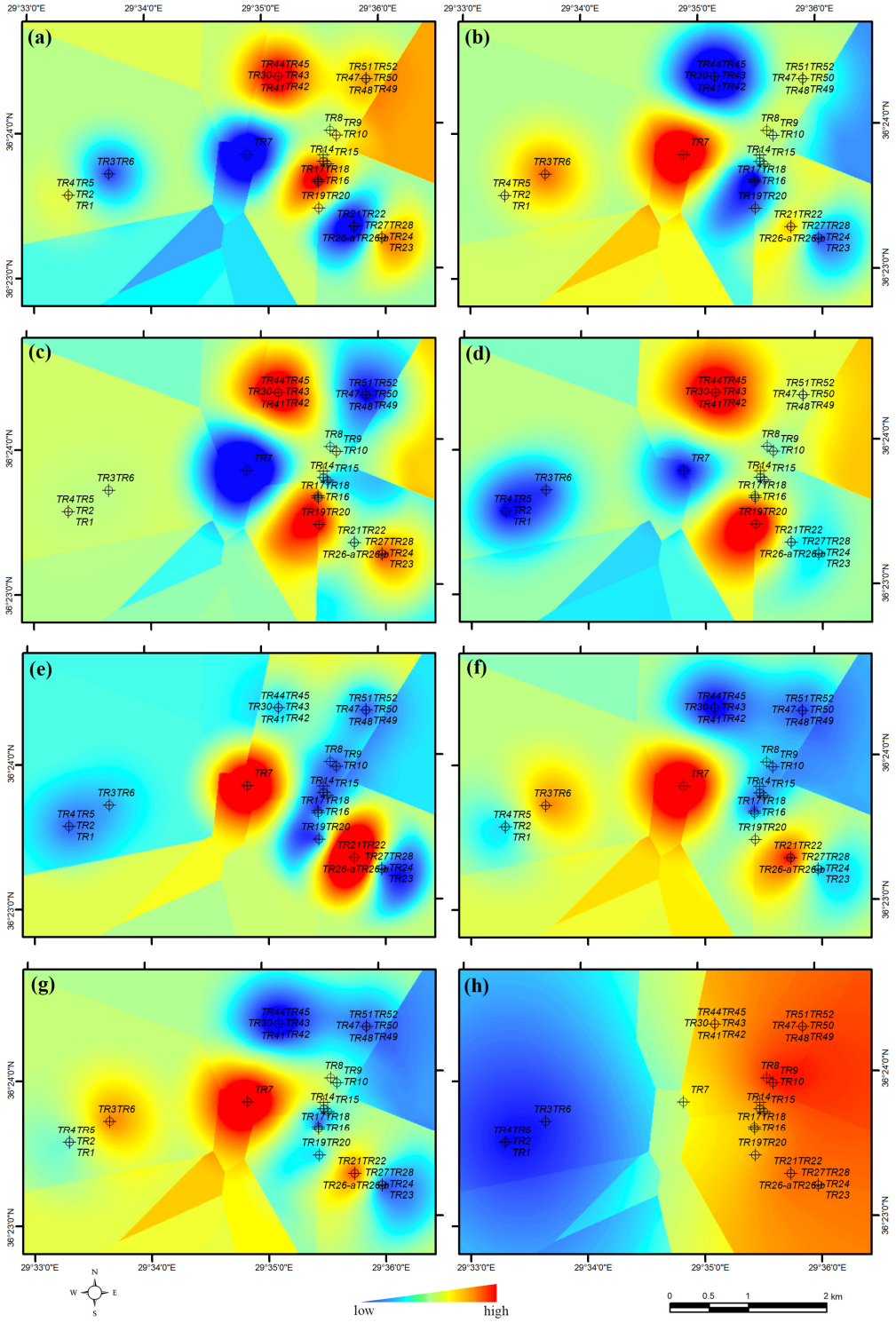


Figure 4. Spatial distribution maps of the major element oxide concentrations of the red soil samples: (**a**) Al_2O_3, (**b**) SiO_2, (**c**) Fe_2O_3, (**d**) TiO_2, (**e**) CaO, (**f**) MgO, (**g**) K_2O, and (**h**) Mn.

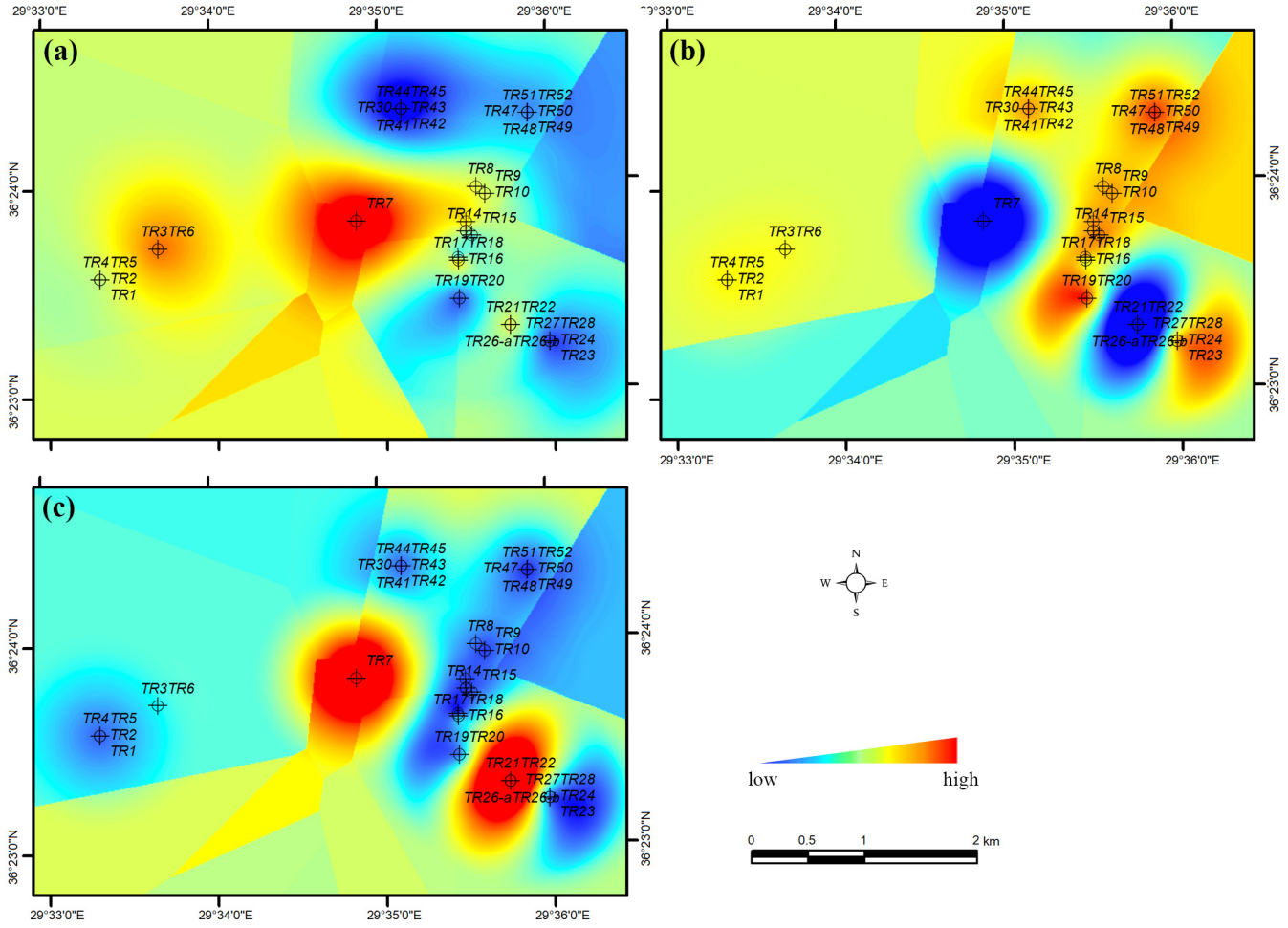


Figure 5. Spatial distribution maps of the trace element concentrations of the red soil samples (**a**) Rb, (**b**) CIW, and (**c**) PIA.

4.2. Statistical Analyses

4.2.1. Descriptive Statistics

The results of the chemical analysis of the red soil samples, and the mean values ± standard errors of the major elements are listed in descending order as follows: Al_2O_3 (45.40 ± 1.06) > SiO_2 (30.58 ± 1.01) > Fe_2O_3 (17.45 ± 0.36) > TiO_2 (2.64 ± 0.05) > CaO (0.60 ± 0.10) > MgO (0.52 ± 0.04) > K_2O (0.38 ± 0.03) > P_2O_5 (0.26 ± 0.01) > SO_3 (0.09 ± 0.005). On the other hand, the mean values ± standard errors of the trace elements are listed in descending order as follows: Mn (1056.53 ± 77.86) > Cr (580.69 ± 20.75) > V (439.48 ± 40.80) > Co (430.00 ± 7.93) > Sr (407.53 ± 32.97) > Ni (312.11± 13.24) > Zn (294.12 ± 6.59) > Ce (222.18 ± 10.27) > Y (147.99 ± 9.09) > La (128.84 ± 10.54) > Cu (120.12 ± 4.85) > Nb (110.74 ± 2.64) > Ba (100.30 ± 9.48) > Pb (94.27 ± 2.31) > Cl (77.61 ± 2.49) > As (67.80 ± 2.47) > Th (61.66 ± 10.22)> Ga (54.67 ± 1.85) > Hf (39.81 ± 4.68) > Sn (39.62 ± 1.13) > Rb (31.74 ± 2.40) > W (17.28 ± 4.36) > U (10.75 ± 0.63).

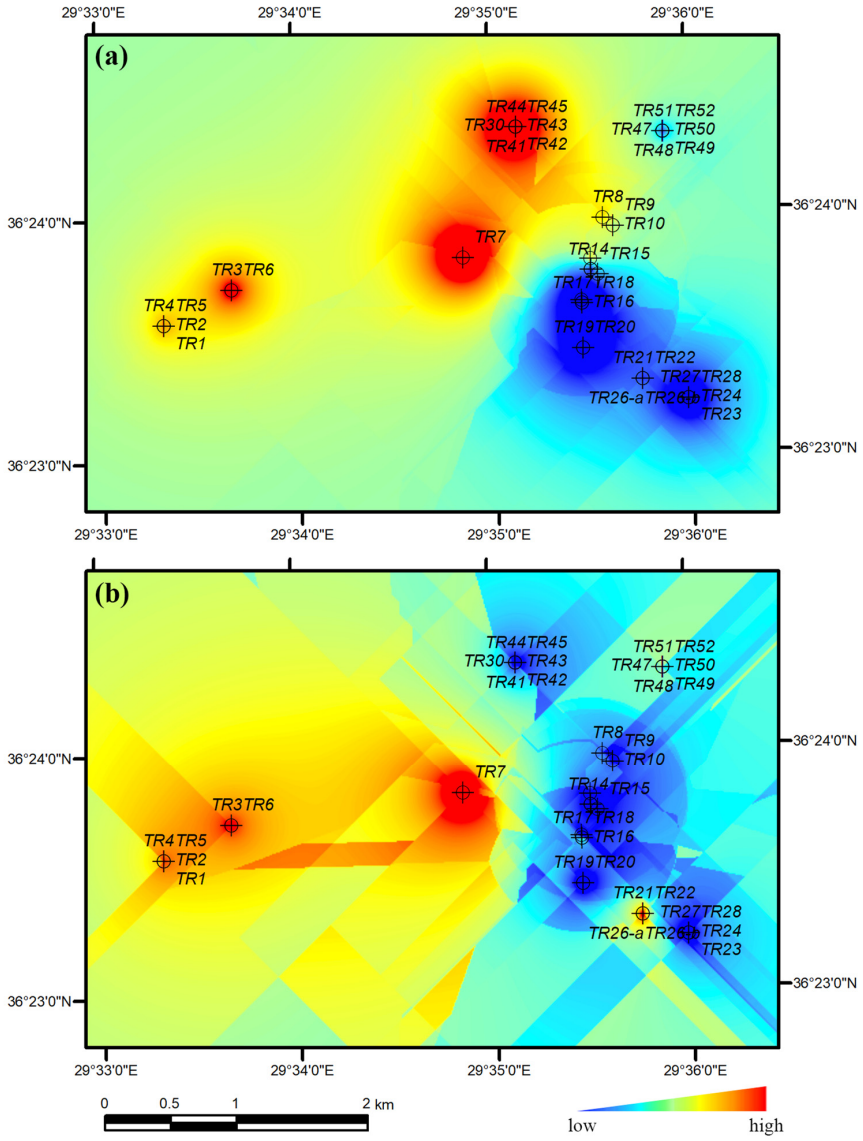


Figure 6. Spatial distribution maps of (**a**) R-Al_2O_3 (strong negative correlation) and (**b**) PIA-CaO (strong positive correlation).

4.2.2. Correlation Analysis

Red soil samples, which are formed in nature depending on environmental conditions and geological environment characteristics, basically consist of a combination of elemental compositions. Red soil samples were formed with the increase in major and trace elements such as Al_2O_3, Mn, Cr, Y, Ce, and Rb, as the concentrations of oxide compounds such as SiO_2, CaO, SO_3, K_2O, P_2O_5, MgO, which are among the rock-forming components, decreased due to geological environment properties and their concentrations. An in-depth investigation of these elemental relationships is important for the determination of the genetic properties of the red soils in the region. Elemental relationships were extracted by Pearson correlation analysis. Elements that are enriched together in the formation environment and depleted in the environment with negative and positive correlations have been learned. It can be assumed that the data used in the study, of about 49 red soil samples, are normally distributed according to the central limit theorem [39–51]. A correlation table was prepared using the equation of Pearson's correlation coefficient for the data assumed to be normally distributed (Table 3). The results of Pearson's correlation analysis are summarized as follows.

Table 3. Pearson's correlation coefficient table according to the results of the chemical analysis and alteration indices.

	MgO	**Al_2O_3**	**SiO_2**	**P_2O_5**	**SO_3**	**Cl**	**K_2O**	**CaO**	**TiO_2**	**Fe_2O_3**	**Br**	**V**	**Cr**	**Mn**	**Co**	**Ni**	**Cu**	**Zn**	**Ga**	**Ge**	**As**	**Se**	**Rb**	**Sr**	**Y**	**Nb**	**Cd**	**In**	**Sn**	**Sb**	**Te**	**Ba**	**La**	**Ce**	**Hf**	**Ta**	**W**	**Pt**	**Ir**	**Au**	**Tl**	**Hg**	**Pb**	**Bi**	**Th**	**U**	**CIA**	**CIW**	**PIA**	**R**
MgO	1	−0.540 **	0.615 **	−0.236	0.594 **	0.523 **	0.922 **	0.484 **	0.225	−0.429 **	0.722 **	−0.075	−0.480 **	0.139	−0.398 **	0.060	−0.125	−0.042	−0.356 *	−0.058	−0.200	−0.213	0.819 **	−0.311 *	−0.217	−0.578 **	0.014	−0.206	−0.277 *	−0.130	−0.133	0.608 **	−0.205	−0.477 **	−0.123	−0.035	−0.092	0.054	0.103	−0.227	0.081	−0.278 *	−0.566 **	−0.279 *	−0.031	−0.621 **	−0.573 **	−0.298 *	0.741 **	0.171
Al_2O_3		1	−0.479 **	0.026	−0.285 *	−0.185	−0.510 **	−0.261	−0.093	0.223	−0.305 *	0.008	0.384 **	0.141	0.330 *	−0.091	0.028	−0.020	0.246	0.040	0.141	−0.144	−0.431 **	0.066	0.077	0.566 **	−0.343 *	−0.231	0.190	−0.064	0.208	−0.370 **	0.350 *	0.447 **	0.036	0.071	0.093	0.096	−0.025	0.234	0.031	0.051	0.484 **	0.048	0.043	0.353 *	−0.139	−0.490 **	−0.400 **	−0.888 **
P_2O_5				1	0.283 *	−0.112	−0.363 **	0.042	0.128	0.274	−0.407 **	−0.202	0.562 **	−0.041	0.269	0.058	0.290 *	0.327 *	−0.059	−0.124	−0.041	0.012	−0.429 **	0.745 **	0.386 **	0.537 **	−0.070	−0.064	−0.087	0.120	0.024	0.100	0.427 **	0.399 **	0.041	0.156	−0.182	−0.023	0.151	0.208	0.037	0.155	0.479 **	−0.129	0.057	0.537 **	0.378 **	0.287 *	−0.058	0.040
K_2O							1	0.440 **	0.153	−0.503 **	0.790 **	−0.105	−0.579 **	0.090	−0.447 **	0.082	−0.107	−0.029	−0.295 *	−0.107	−0.286 *	−0.178	0.945 **	−0.334 *	−0.215	−0.606 **	−0.015	−0.165	−0.258	−0.240	−0.138	0.590 **	−0.225	−0.529 **	−0.206	−0.104	−0.111	0.125	0.037	−0.250	0.107	−0.348 *	−0.600 **	−0.221	−0.045	−0.723 **	−0.620 **	−0.333 *	0.682 **	0.146
CaO								1	0.034	−0.247	0.531 **	−0.141	−0.053	0.102	−0.221	−0.021	−0.087	−0.124	−0.082	−0.088	−0.090	−0.068	0.327 *	−0.046	−0.126	−0.256	0.006	−0.086	−0.179	−0.115	−0.152	0.328 *	0.032	−0.196	−0.094	−0.118	−0.045	0.112	−0.064	−0.343 *	−0.048	−0.132	−0.221	−0.161	−0.118	−0.207	−0.717 **	−0.533 **	0.946 **	0.052
Fe_2O_3										1	−0.578 **	0.220	0.646 **	0.256	0.773 **	−0.098	−0.260	0.155	0.257	0.021	0.352 *	0.297 *	−0.551 **	−0.126	−0.313 *	0.476 **	−0.408 **	0.218	0.355 *	0.370 **	0.025	−0.221	0.190	0.645 **	−0.239	0.075	0.049	0.106	−0.081	0.564 **	0.024	0.296 *	0.632 **	0.139	0.110	0.744 **	0.424 **	0.309 *	−0.350 *	−0.009
Br											1	−0.067	−0.535 **	−0.073	−0.382 **	0.068	−0.035	−0.301 *	−0.287 *	−0.130	−0.310 *	−0.279 *	0.731 **	−0.226	−0.121	−0.569 **	−0.030	−0.164	−0.313 *	−0.229	−0.200	0.338 *	−0.246	−0.552 **	−0.267	−0.202	0.279 *	0.032	0.022	−0.545 **	−0.058	−0.416 **	−0.590 **	−0.127	0.024	−0.663 **	−0.688 **	−0.462 **	0.677 **	0.030
Cr												1	0.293 *	−0.076	0.664 **	−0.148	−0.128	0.003	0.108	−0.094	0.157	0.142	−0.683 **	0.293 *	−0.076	0.664 **	−0.302 *	−0.065	0.092	0.040	0.137	−0.048	0.519 **	0.819 **	0.034	0.126	−0.106	0.118	0.040	0.496 **	0.052	0.348 *	0.765 **	0.008	0.074	0.830 **	0.271	0.092	−0.221	−0.215

Table 3. *Cont.*

	MgO	Al_2O_3	SiO_2	P_2O_5	SO_3	Cl	K_2O	CaO	TiO_2	Fe_2O_3	Br	V	Cr	Mn	Co	Ni	Cu	Zn	Ga	Ge	As	Se	Rb	Sr	Y	Nb	Cd	In	Sn	Sb	Te	Ba	La	Ce	Hf	Ta	W	Pt	Ir	Au	Tl	Hg	Pb	Bi	Th	U	CIA	CIW	PIA	R
Ga																			1	0.003	0.179	0.160	−0.204	−0.067	−0.004	0.198	−0.171	0.164	0.707 **	0.247	0.190	−0.156	0.019	0.218	−0.237	−0.097	0.093	−0.173	−0.175	0.119	0.062	−0.070	0.094	0.283 *	−0.499 **	0.190	0.106	0.029	−0.194	−0.087
Rb																							1	−0.324 *	−0.180	−0.630 **	0.037	−0.171	−0.247	−0.295 *	−0.188	0.550 **	−0.213	−0.580 **	−0.204	−0.197	−0.106	0.150	−0.023	−0.271	0.162	−0.421 **	−0.655 **	−0.164	−0.095	−0.789 **	−0.570 **	−0.315 *	0.558 **	0.104
Sr																								1	0.773 **	0.406 **	0.069	−0.085	−0.163	−0.031	0.039	−0.012	0.271	0.154	0.117	0.194	−0.113	−0.093	0.190	−0.073	−0.080	0.016	0.256	−0.099	−0.081	0.310 *	0.324 *	0.236	−0.151	0.040
Nb																									1	−0.425 **	−0.017	0.241	0.082	0.228	−0.424 **	0.517 **	0.678 **	0.019	0.217	−0.058	0.031	0.052	0.373 **	−0.057	0.346 *	0.866 **	0.134	0.135	0.636 **	0.336 *	0.100	−0.412 **	−0.326 *
Cd																										1	0.100	−0.244	0.010	−0.164	0.171	−0.122	−0.273	0.722 **	−0.140	−0.043	−0.077	0.011	−0.179	−0.016	−0.057	−0.387 **	−0.022	−0.127	−0.152	0.120	0.186	0.009	0.320 *
Ce																																	1	0.040	0.134	−0.115	0.120	0.036	0.622 **	0.077	0.319 *	0.780 **	0.080	0.081	0.732 **	0.280 *	0.088	−0.329 *	−0.270
Pb																																										1	0.057	0.181	0.721 **	0.344 *	0.135	−0.381 **	−0.252
CIA																																													1	0.924 **	−0.764 **	0.464 **
CIW																																													1	−0.521 **	0.754 **

*. Correlation is significant at the 0.05 level (2-tailed). **. Correlation is significant at the 0.01 level (2-tailed).

There is a very strong positive correlation between K_2O and MgO, which are the major elemental contents of the red soil samples (0.922 **). In addition, K_2O and MgO have a moderate positive correlation with Br, which is one of the trace elements (0.790 **, 0.722 **). Sr, which is one of the trace elements, has a moderate positive correlation with P_2O_5, which is one of the major elements, and Y, which is one of the trace elements, (0.745 **, 0.773 **). There is a moderate positive correlation between Sn and Ga, which are trace elements, (0.707 **). There is a strong positive correlation between Ce and Cr, which are trace elements, (0.819 **). While Pb, which is a trace element, has a moderate positive correlation with Cr and Ce, which are also trace elements, and it has a strong positive correlation with Nb (0.765 **, 0.866 **, 0.780 **). There is a strong negative correlation between R (Ruxton ratio), which is one of the chemical weathering indices, and the major elemental content of Al_2O_3 −0.888 **). There is a strong positive correlation between the plagioclase index of alteration (PIA), which is one of the chemical weathering indices, and the major elemental content of CaO (0.946 **). There is a strong positive correlation between the chemical index of weathering (CIW) and the chemical index of alteration (CIA) (0.924 **).

4.2.3. Regression Analysis

The strong positive and negative correlations were revealed by the correlation analysis. Some correlations were also determined between the results of the elemental analysis of the red soil samples and the index values, which revealed the paleoclimatic characteristics. Therefore, the statistical explanation of the aforementioned correlations was also tested by using simple linear regression analysis. The scatter diagrams of the correlations were plotted under three models (Figure 7): (R-Al_2O_3), (PIA-CaO), and (CIW-CIA). Regarding the chemical formation models of the red soil samples, R^2 (coefficient of determination), statistical errors, and coefficient predictions are given in Tables 4–6.

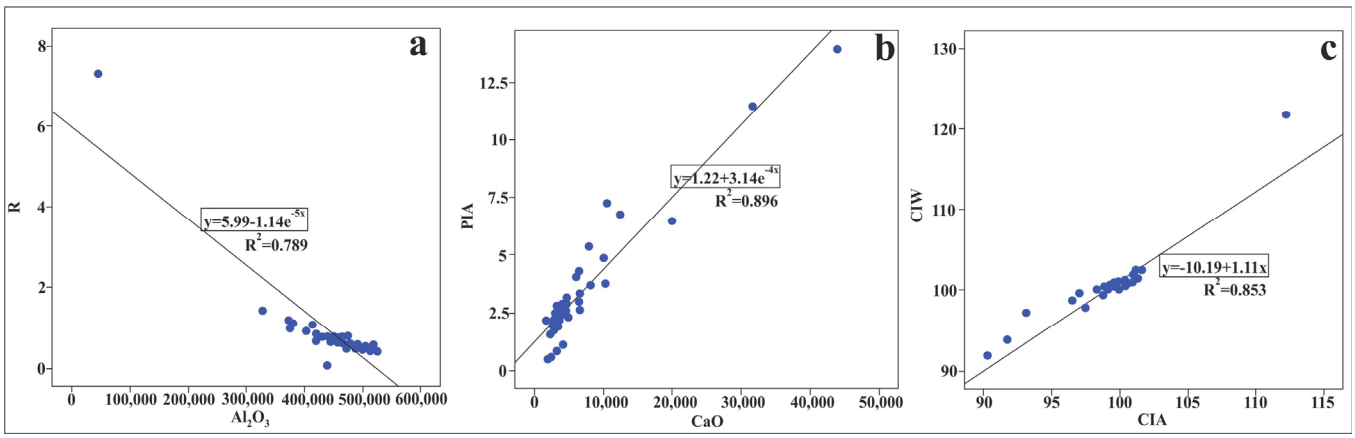


Figure 7. Scatter Diagrams: (**a**) R-Al_2O_3, (**b**) PIA-CaO, (**c**) CIW-CIA.

Table 4. Coefficient of determination (explained variance) table of the models.

Model Summary [b]				
Model	**R**	**R Square**	**Adjusted R Square**	**Std. Error of the Estimate**
1	0.88 [a]	0.78	0.78	34,417.82
2	0.94 [a]	0.89	0.89	2387.50
3	0.92 [a]	0.85	0.85	1.12

[a]. Predictors: (Constant). R (Model 1); PIA (Model 2); CIW (Model 3). [b]. Dependent Variable: Al_2O_3 (Model 1); CaO (Model 2); CIA (Model 3).

Table 5. Statistical error (analysis of variance) table of the models.

ANOVA [a]						
Model		**Sum of Squares**	**df**	**Mean Square**	**F**	***p*-Value**
1	Regression	216,969,266,475.20	1	216,969,266,475.20	183.16	0 [b]
	Residual	58,044,733,524.79	49	1,184,586,398.46		
	Total	275,014,000,000.00	50			
2	Regression	2,396,218,278.45	1	2,396,218,278.45	420.37	0 [b]
	Residual	279,308,450.95	49	5,700,172.46		
	Total	2,675,526,729.41	50			
3	Regression	358.66	1	358.66	284.97	0 [b]
	Residual	61.67	49	1.25		
	Total	420.34	50			

[a]. Predictors: (Constant). R (Model 1); PIA (Model 2); CIW (Model 3). [b]. Dependent Variable: Al_2O_3 (Model 1); CaO (Model 2); CIA (Model 3).

Table 6. Table of the coefficients of the mathematical models.

Coefficients [a]						
Model		**Unstandardized Coefficients**		**Standardized Coefficients**	**t**	***p*-Value**
		B	**Std. Error**	**Beta**		
1	(Constant) (b_0)	508,476.83	6375.07		79.76	0
	R (b_1)	−68,989.86	5097.64	−0.88	−13.53	0
2	(Constant) (b_0)	−2846.49	550.81		−5.16	0
	PIA (b_1)	2851.50	139.07	0.94	20.50	0
3	(Constant) (b_0)	22.462	4.586		4.898	0
	CIW (b_1)	0.767	0.045	0.92	16.881	0

[a]. Predictors: (Constant). R (Model 1); PIA (Model 2); CIW (Model 3). Dependent Variable: Al_2O_3 (Model 1); CaO (Model 2); CIA (Model 3).

Model 1 gives a linear negative correlation between Al_2O_3–R, while Model 2 gives a linear positive correlation between PIA–CaO, and Model 3 gives a linear positive correlation between CIA–CIW. The R^2 value of Model 1 is 0.78, the *p*-value of the model is 0, and the *p*-value of the b_0 is lower than 0.05. The R^2 value of Model 2 is 0.89, the *p*-value of the model is 0, and the *p*-value of the b_0 is lower than 0.05. The R^2 value of Model 3 is 0.85, the *p*-value of the model is 0, and the *p*-value of the b_0 is lower than 0.05. The explained variances in the mathematical models proposed for red soil formations are high. The probability value obtained from the ANOVA analysis of each model is 0. The parameter estimates of the mathematical equations designed for each model are below 0.05 [52–55]. These models explain the chemical formation model at the significance level of 0.05.

4.2.4. Factor Analysis

Factor analysis was conducted to determine the variances in the correlations that were found to be statistically significant in the correlation table [56–62]. The Kaiser–Meyer–Olkin test was conducted to evaluate the suitability of the data for factor analysis [63–66] (Table 7).

Table 7. Kaiser–Meyer–Olkin (KMO) measure of sampling adequacy.

KMO and Bartlett's Test	
Kaiser–Meyer–Olkin Measure of Sampling Adequacy.	0.573

The data were found to be suitable for factor analysis, and the sampling adequacy measure was found to be greater than 0.5 [67–73]. The number of factors under which the data were collected was interpreted using the scree plot (Figure 8). The variances of these factors are given in Table 8.

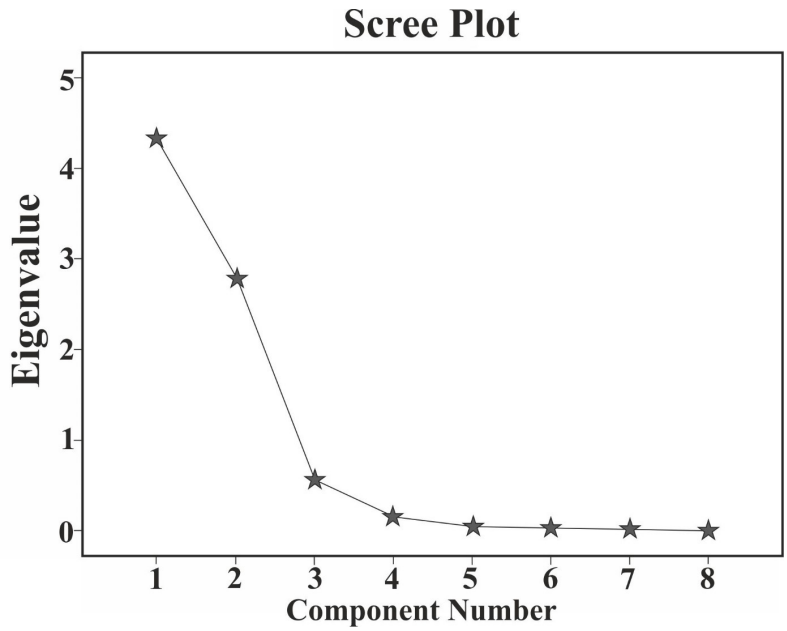


Figure 8. Scree plot of the factor analysis.

Table 8. Total variance explained.

Total Variance Explained						
Component	**Initial Eigenvalues**			**Extraction Sums of Squared Loadings**		
	Total	**% of Variance**	**Cumulative %**	**Total**	**% of Variance**	**Cumulative %**
1	4.3	54.32	54.32	4.34	54.32	54.32
2	2.8	35.16	89.48	2.81	35.16	89.48
3	0.58	7.25	96.73			
4	0.16	2.06	98.80			
5	0.04	0.54	99.35			
6	0.02	0.35	99.70			
7	0.02	0.28	99.99			
8	0.001	0.01	100			

Extraction method: principal component analysis.

The scree plot reveals that the slope of the plot begins to disappear between two and three. According to the table that presents the variances in the factors, the data are explained under two factors, with an eigenvalue greater than one. While Factor 1 explains 54.32% of the total variance, Factor 1 and Factor 2 cumulatively explain 89.48% of the total variance. The cumulative variances in the geochemical data and indices were calculated. Principal component analysis (PCA) was conducted to learn the components of the obtained factors. The components and variances explained by each factor were found as follows: The geochemical compounds and the indices used for paleoclimatic interpretations that explained Factor 1 were found to be MgO, K_2O, Rb, and PIA, and the explained variance was found to be 54.32%. The geochemical compounds and the indices used for paleoclimatic interpretations that explained Factor 2 were found to be CIA, CIW, and R, and the explained variance was found to be 35.16% (Table 9). As can be clearly seen in the principal components' matrix, the major element of Al_2O_3 did not correlate with any factor (Figure 9).

Table 9. Component matrix table.

Component Matrix [a]		
	Component	
	1	2
Al_2O_3	−0.39	−0.89
MgO	0.91	0.22
K_2O	0.94	0.19
Rb	0.87	0.16
PIA	0.85	0.004
CIA	−0.81	0.54
CIW	−0.55	0.81
R	0.008	0.96
% of Variance	54.32	35.16

Extraction method: principal component analysis. [a]. Two components extracted.

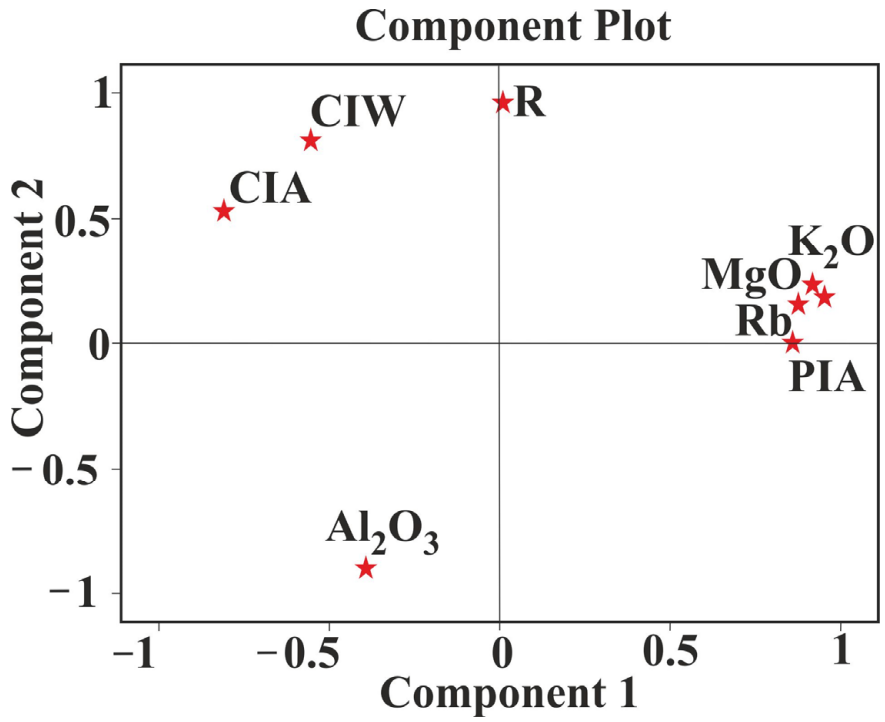


Figure 9. Principal components plot.

4.2.5. Cluster Analysis

The red soil samples were classified according to their geochemical and paleoclimatic index properties by using hierarchical clustering analysis (Figure 10). The heat map method was used to understand the distribution of nominal variables with numerical variables [51]. The distribution of the geochemical and paleoclimatic index properties of the red soil samples at different laterization degrees was obtained using the heat map (Figure 11).

The hierarchical clustering analysis revealed that the red soil samples were classified into three groups according to the geochemical and paleoclimatic index data. The major oxide elements of TiO_2, CaO, MgO, K_2O, P_2O_5, and SO_3, the trace elements of Mn, Cr, Co, V, Sr, Ni, Zn, Ce, Y, La, Cu, Nb, Ba, Pb, Cl, As, Th, Ga, Hf, Sn, Rb, W, U, Au, Pt, Br, Sb, Ta, Hg, Cd, and Te, and the indices of PIA, CIA, CIW, and R constituted Group 1. The major oxide elements of Fe_2O_3 and SiO_2 constituted Group 2. Al_2O_3, a major element, which behaved differently from other elements and weathering indices, constituted Group 3.

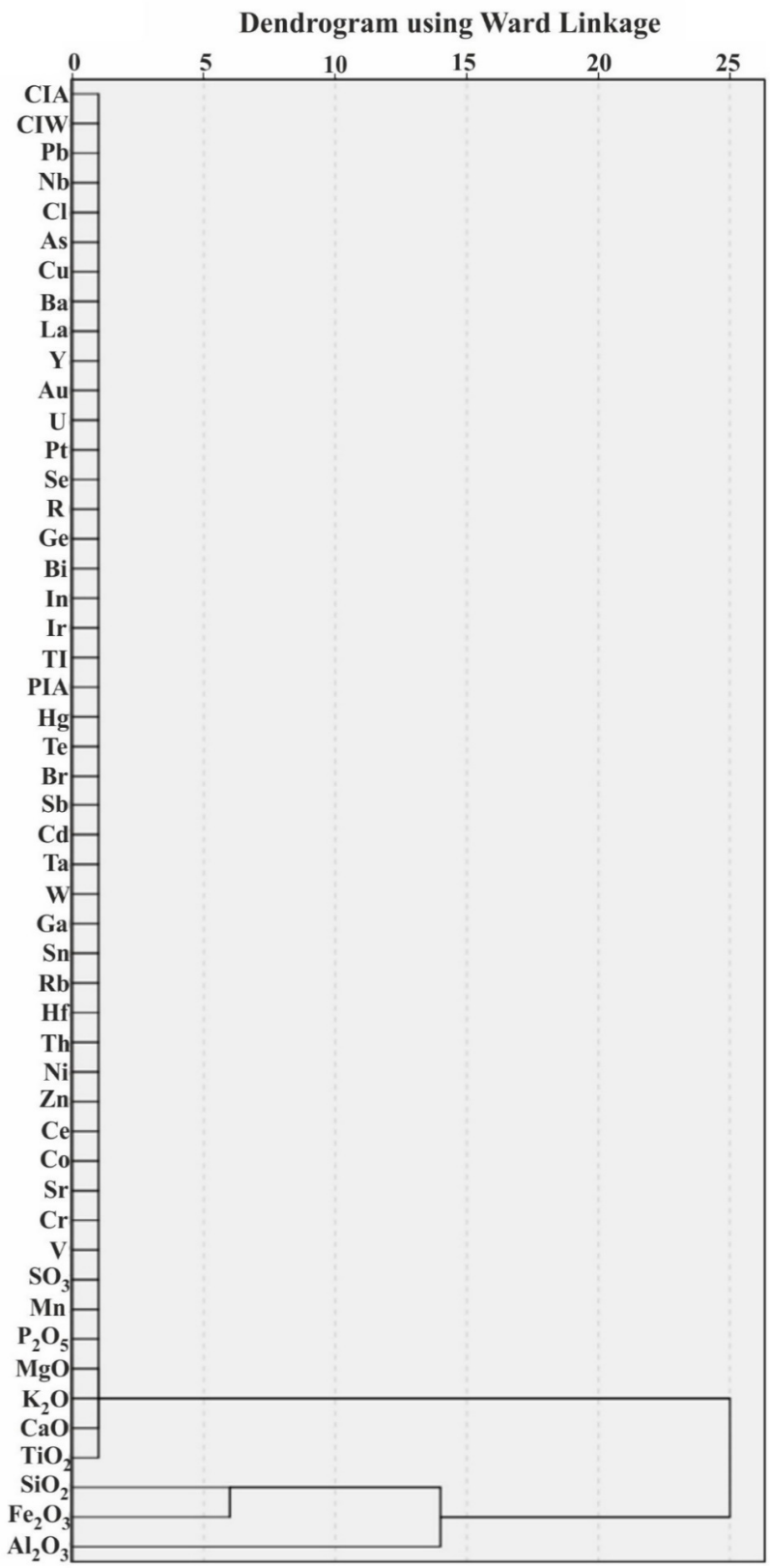


Figure 10. Hierarchical clustering of the variables.

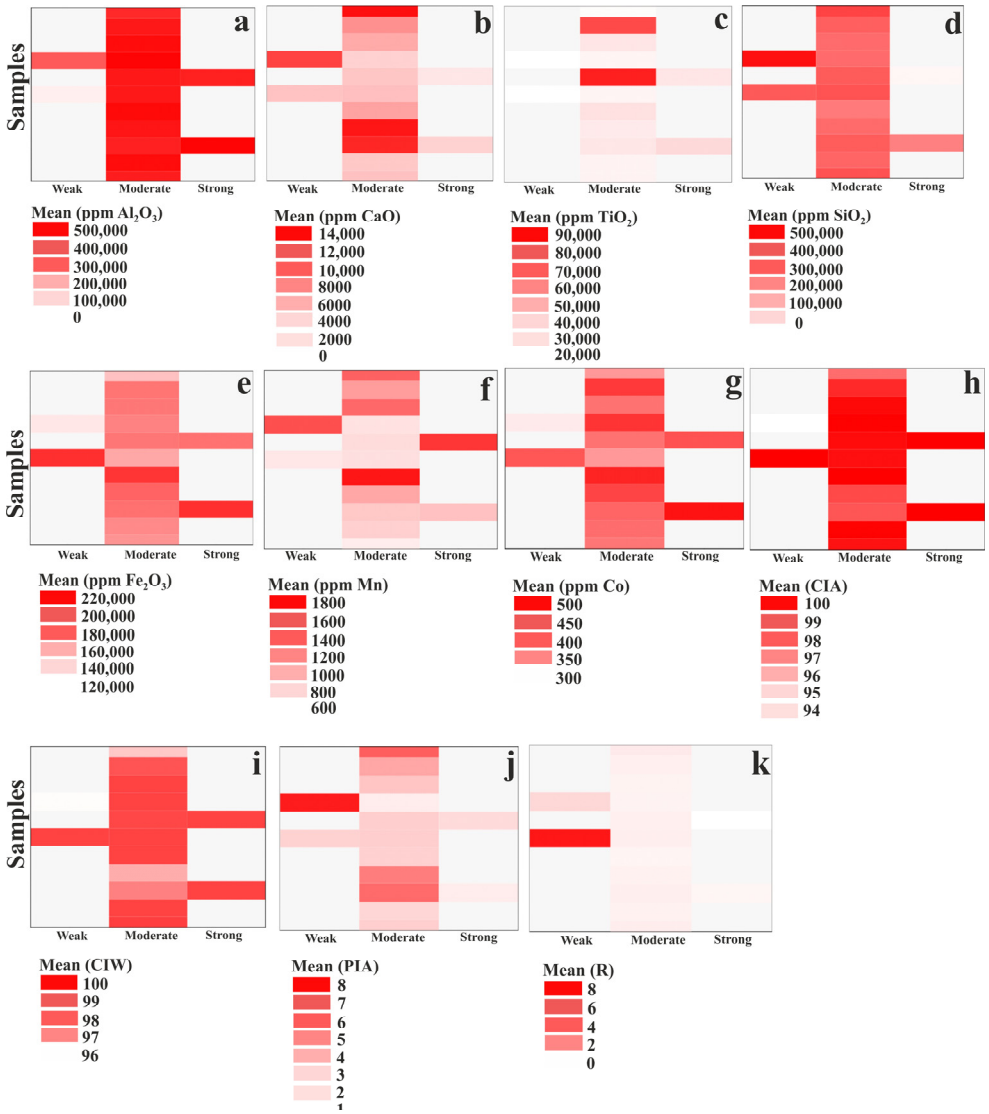


Figure 11. Heat-map classification of the geochemical data and the paleoclimatic indices (**a**) Al_2O_3; (**b**) CaO; (**c**) TiO_2; (**d**) SiO_2; (**e**) Fe_2O_3; (**f**) Mn; (**g**) Co; (**h**) CIA; (**i**) CIW; (**j**) PIA; (**k**) R.

The red soil that has undergone a weak laterization reaction has lower Al_2O_3, TiO_2, and CaO contents. The red soil that has undergone a moderate laterization reaction has lower geochemical contents of TiO_2 and Mn, and index values of PIA and R. The red soil that has undergone a high level of laterization reaction has lower geochemical contents of CaO, TiO_2, and SiO_2, and index values of PIA and R.

5. Discussion

Due to the high topographical variation in the land and the difficulty of access in the forest area, the sampling procedures were obtained from the best possible locations, and in a way that best represents the land. Comparisons of sample results in the international literature are briefly summarized. According to the results of the chemical analysis of the red soil samples collected from western Sicily, the major elemental contents were found to be Al_2O_3, Fe_2O_3, and TiO_2, while the trace elemental contents were found to be Cu, Cr, Cd, Pb, Mn, Zn, and Ni. The values of these elements were observed in the following ranges: Cd, 0.85–1.9 ppm; Cu, 30–37 ppm; Cr, 94–129 ppm; Mn, 86–2222 ppm; Ni, 49–68 ppm; Pb, 32–43 ppm; Zn, 109–166 ppm [8]. The ranges of the above-mentioned elements observed in the red soil samples collected from the Sutlegen area are as follows: Cd, 0–56.2 ppm;

Cu, 81.8–268 ppm; Cr, 335–892 ppm; Mn, 449–3730 ppm; Ni, 0–472 ppm; Pb, 59.6–133 ppm; Zn, 198–396 ppm. According to these values, the trace element concentrations of western Sicily red soil samples were found to be lower than those of the Sutlegen red soil samples.

The major elements of the red soil samples collected from the Guizhou Plateau in southern China included Al_2O_3, SiO_2, Fe_2O_3, CaO, MgO, K_2O, and Al_2O_3, and the trace elements included Sr, Y, Zr, Nb, Ba, Zn, Ni, Cu, and V. The chemical indices of alteration (CIA) values calculated using the major element contents of the red soil samples were found to range between 72 and 89 [1]. According to the results of the geochemical analysis conducted for the red soil samples collected from Seydisehir in Konya (Türkiye), the CIA values were found to range between 85 and 97. According to the geochemical analysis results of Seydisehir red soil samples, the CIA values ranged between 90.30 and 100. On the other hand, the values of the chemical index of alteration (CIA) calculated for the Sutlegen red soil samples were found to range between 90.3 and 100.

The red soil samples collected from the Jubaila formation in Saudi Arabia were subjected to chemical analysis. According to the results of the chemical analysis, the major element contents were found to be SiO_2, Al_2O_3, Fe_2O_3, CaO, MgO, Na_2O, K_2O, TiO_2, MnO, and P_2O_5. The chemical index of alteration (CIA) values, calculated using the values of the major elements, were found to range between 25 and 84 [10]. The CIA values calculated for the Sutlegen red soil samples were found to be higher than the CIA values calculated for the red soil samples collected from the Jubaila formation in Saudi Arabia.

According to the results of the chemical analysis of the red soil samples collected from the Chinese Tibetan Plateau, the concentrations of the major elements were found in the following order: SiO_2 > CaO > Fe_2O_3 > Al_2O_3 > K_2O > MgO > TiO_2 > Na_2O > P_2O_5 > MnO [20]. On the other hand, the concentrations of the major elements in the Sutlegen red soil samples were found in the following order: Al_2O_3 > SiO_2 > Fe_2O_3 > TiO_2 > CaO > MgO > K_2O > P_2O_5 > SO_3.

The concentrations of the significant major and trace elements in the red soil samples collected from the Karaman province (Türkiye) were found to be in the following ranges: Si (90,735.05–211,715.1 ppm), Al (115,689.1–228,202.7 ppm), Fe, (69,663.87–118,134.8 ppm), Mn (1161.69–1548.91 ppm), Cr (166.4–254.8 ppm), and Co (26.8–85.9) [4,40–43]. Considering the ranges of the above-mentioned major and trace element concentrations in the Sutlegen red soil samples, the concentrations of the Si and Mn elements were observed to be lower while the concentrations of the Al, Fe, Cr, and Co elements were observed to be higher.

In a study conducted on the red soil samples, which were lateritic weathering products, from Southwestern China, the CIA values were calculated using the results of the chemical analysis. The CIA values were found to range between 0.11 and 94.11 [44]. The range of the CIA values of the Sutlegen red soil samples was found to be higher than that of the red soil samples from Southwestern China. Higher CIA values are associated with the intensity of the chemical weathering process. Therefore, the primary minerals in the soil turn into secondary minerals because of chemical alteration [28]. The kaolinite samples, which consist of clay minerals, have a CIA value of 100. The closer the CIA value of the sample is to 100, the higher the kaolinite mineral enrichment is. The shales come in second place, and their CIA values range between 70 and 75. The illites, as one of the clay group minerals, come in third place, and their CIA value is 75. The CIA values of the granites and granodiorites range between 45 and 55 [26–28].

The triangular diagram (modified after [37]), showing the laterization degree of the red soil samples, revealed that they had weak, moderate, and strong laterization reactions. However, it is clearly seen that most of the samples underwent moderate laterization.

The abundance of Ca, Mg, and Sr was determined in the geochemical study carried out on the red clays formed on the river delta. Clays that have undergone the physical processes of weathering, sorting, dilution, and adsorption are characterized by red colors. The sediment transport along the delta has brought along geochemical differentiation [74]. Red soils are heavily weathered soils. They contain secondary minerals with high Fe and Al content. However, soils that have not undergone high weathering and are characterized as

more yellow to brown in color are rich in primary minerals with K and Si content [75]. As the degree of decomposition in the soil increases (CIA, CIW, PIA, R), the color is characterized by red tones and the soil is enriched with secondary minerals. The distribution of heavy metals in soil samples collected from the karst terrain Guilin region in southwestern China was studied. Located on a karstic terrain, the Guilin region consists of carbonate and clastic rocks. A total of 11 heavy metal contents were extracted from the soil profiles collected from the field. The factors affecting them are discussed. It has been determined that heavy metals are enriched in the soil mainly by secondary mineralization. By using Pearson correlation analysis, the physical and chemical parameter relations of calcareous soils and red soil samples were determined. For the red soil samples collected at different depths, it was determined that Mo decreased as the depth increased. It was observed that Fe and Mn contents were found in high concentrations in karstic soil samples. Red soils showed higher Mo, Pb, and Sr contents than calcareous soils [76].

The red soil samples from the Sutlegen Village were compared with other red soil samples reported in the literature (Table 10) [6]. Compared to red soil samples collected from Ibradi and Seyrandagi, the concentrations of Al_2O_3, Fe_2O_3, TiO_2, V, Zn, Sr, Y, Nb, Ce, Pb, and Th elements were observed to be higher.

Table 10. Comparison between major and trace element geochemical analyses of samples collected from Ibradi and Seyrandagi red soils with Sutlegen Kas red soil samples [6].

	Red Soil in the Ibradi Group	**Red Soil in the Seyrandagi Limestone**	**Antalya, Kas Sutlegen Red Soil (This Study)**
Major oxides (%)			
Al_2O_3	10.56–23.33	14.31–22.86	4.50–53.80
SiO_2	46.60–73.40	47.31–67.63	3.20–46.90
Fe_2O_3	04.96–10.79	05.95–09.69	11.00–21.40
CaO	00.16–00.68	00.68–01.30	0.17–4.39
MgO	01.08–05.16	01.29–02.87	0.00–1.55
K_2O	01.34–02.41	01.83–02.21	00.08–1.46
TiO_2	00.64–01.03	00.83–01.21	1.92–3.57
P_2O_5	00.09–00.36	00.14–00.55	00.03–00.48
Trace Elements (ppm)			
V	96–195	120–288	0–987
Ni	100–379	148–239	1–72
Cu	53–133	62–101	6–41
Zn	53–147	87–260	198–396
Rb	47–110	71–125	8–92
Sr	44–144	56–242	37–1140
Y	23–80	44–77	81–358
Nb	11–22	15–27	65–144
Ce	76–146	88–191	0–365
Pb	31–44	33–53	59–133
Th	6–13	7–17	0–546

6. Conclusions

In this study, the characterization of the formation model of red soil samples collected from the study area was investigated using the geological aspect of the study area, calculating various index values, performing multivariate statistical analysis, and determining their spatial distribution. This differentiation indicated that the red soil formations in the region were associated with magmatic fluids. It was thought that the red soil on the carbonate and non-carbonate rocks in the region was formed due to magmatic and metamagmatic rocks that are possibly buried in the region or outcropped in the close vicinity, and it has an autochthonous formation particularly due to magmatic fluids affecting the region. The chemical composition of red soils is compatible with bauxite ore. The alteration development of the rocks or formations in the region is also suitable for bauxite forma-

tion. Therefore, it is thought that bauxite ore is present in the region. Detailed mineral exploration should be carried out in and around the study area.

Author Contributions: In this research article, O.O.A. and M.G.Y. prepared the methodology and conceptualization. O.O.A. performed the analyses and interpreted the results of the analyses. The field study was performed by M.G.Y. and O.O.A., while B.T.S., O.O.A. and Y.L. prepared the spatial distributions and figures and interpreted the data. All authors have read and agreed to the published version of the manuscript.

Funding: The Scientific Research Projects Coordination Unit of Akdeniz University, Antalya/Türkiye provided financial support for this research (BAP, FKA-2019-4636). The authors would like to thank the Scientific Research Projects Coordination Unit of Akdeniz University for their financial support.

Acknowledgments: This manuscript is part of the M.Sc. thesis of Atakoglu Ozer O., the first author.

Conflicts of Interest: The authors declare no conflict of interest.

References

1. Cao, X.; Wu, P.; Cao, Z. Element Geochemical Characteristics of a Soil Profile Developed on Dolostone in Central Guizhou, Southern China: Implications for Parent Materials. *Acta Geochim.* **2016**, *35*, 445–462. [CrossRef]
2. Liankai, Z.; Hongbing, J.; Shijie, W.; Gang, L.; Xiuming, L.; Xiao, W.; Dai Trung, N. Geochemical Implications of Rare Earth Elements in Terra Rossa in Tropical Karst Area: A Case Study in Northern Vietnam. *Appl. Sci.* **2020**, *10*, 858. [CrossRef]
3. Yalcin, M.G.; Temur, S. Geochemistry of the Terra Rossa from Ayrancı, Central Turkey. *Geochim. Cosmochim. Acta* **2006**, *18*, 716. [CrossRef]
4. Yalcin, M.G.; Ilhan, S. Major and Trace Element Geochemistry of Terra Rossa Soil in The Kucukkoras Region, Karaman, Turkey. *Geochem. Int.* **2008**, *46*, 1038. [CrossRef]
5. Unal, M. Toprak Oluşumu ve Ülkemizde Çeşitleri. *Bilim Ve Aklın Aydınlığında Eğitim* **2011**, *134*, 12–18.
6. Iskenderoglu, A. Evaluation of Terra Rossa potential for an unqualified forest area in the Mediterranean region using geochemical and GIS methods: A case study from the Central Taurus, Ibradi, Antalya, Turkey. *Arab. J. Geosci.* **2020**, *13*, 1–16. [CrossRef]
7. Bellanca, A.; Hauser, S.; Neri, R.; Palumbo, B. Mineralogy and Geochemistry of Terra Rossa Soils, Western Sicily: Insights into Heavy Metal Fractionation and Mobility. *Sci. Total Environ.* **1996**, *193*, 57–67. [CrossRef]
8. Bourgault, R.R.; Rabenhorst, M.C. Genesis and Characterization of Manganiferous Soils in The Eastern Piedmont, USA. *Geoderma* **2011**, *165*, 84–94. [CrossRef]
9. Eltom, H.A.; González, L.A.; Alqubalee, A.; Amao, A.O.; Salih, M. Evidence for The Development of a Superpermeability Flow Zone by Bioturbation in Shallow Marine Strata Upper Jubaila Formation, Central Saudi Arabia. *Mar. Pet. Geol.* **2020**, *20*, 104512. [CrossRef]
10. Lucke, B.; Kemnitz, H.; Bäumler, R.; Schmidt, M. Red Mediterranean Soils in Jordan: New Insights in Their Origin, Genesis, and Role As Environmental Archives. *Catena* **2014**, *112*, 4–24. [CrossRef]
11. Smith, B.J.; McAlister, J.J. Mineralogy, Chemistry and Palaeoenvironmental Significance of An Early Tertiary Terra Rossa From Northern Ireland: A Preliminary Review. *Geomorphology* **1995**, *12*, 63–73. [CrossRef]
12. Feng, J.L.; Lin, Y.C.; Gao, S.P.; Zhang, J.F. Enrichment of Trace Elements in Ferromanganese Concretions from Terra Rossa and Their Potential Desorption. *Geochem. J.* **2012**, *46*, 151–161. [CrossRef]
13. Moresi, M.; Mongelli, G. The Relation Between the Terra Rossa and The Carbonate-Free Residue of The Underlying Limestones and Dolostones in Apulia, Italy. *Clay Miner.* **1988**, *23*, 439–446. [CrossRef]
14. Olson, C.G.; Ruhe, R.V.; Mausbach, M.J. The Terra Rossa Limestone Contact Phenomena in Karst, Southern Indiana. *Soil Sci. Soc. Am. J.* **1980**, *44*, 1075–1079. [CrossRef]
15. Cooke, M.J.; Stern, L.A.; Banner, J.L.; Mack, L.E. Evidence for The Silicate Source of Relict Soils on The Edwards Plateau, Central Texas. *Quat. Res.* **2007**, *67*, 275–285. [CrossRef]
16. Sandler, A.; Meunier, A.; Velde, B. Mineralogical and Chemical Variability of Mountain Red/Brown Mediterranean Soils. *Geoderma* **2015**, *239*, 156–167. [CrossRef]
17. Thornbury, W.D. *Principles of Geomorphology*, 2nd ed.; John Wiley Sons, Inc.: New York, NY, USA, 1969; pp. 306–307.
18. Mirabella, A.; Costantini, E.A.C.; Carnicelli, S. Genesis of A Polycyclic Terra Rossa (Chromic Cambisol on Rhodic Nitisol) At The Poggio Del Comune in Central Italy. *Z. Pflanz. Und Bodenkd.* **1992**, *155*, 407–413. [CrossRef]
19. Durn, G.; Ottner, F.; Slovenec, D. Mineralogical and Geochemical Indicators of The Polygenetic Nature of Terra Rossa in Istria, Croatia. *Geoderma* **1999**, *91*, 125–150. [CrossRef]
20. Khadkikar, A.S.; Basavaiah, N. Morphology, Mineralogy and Magnetic Susceptibility of Epikarst- Terra Rossa Developed in Late Quaternary Aeolianite Deposits of Southeastern Saurashtra, India. *Geomorphology* **2004**, *58*, 339–355. [CrossRef]
21. Feng, J.L.; Zhu, L.P. Origin of Terra Rossa on Amdo North Mountain on the Tibetan Plateau, China: Evidence from Quartz. *Soil Sci. Plant Nutr.* **2009**, *55*, 407–420. [CrossRef]

22. Keser, N. Saribelen (Sidek) Polyesi ve Katran Dagi'nin Karst Jeomorfolojisi. In *Marmara Coğrafya Dergisi*; Sayı: İstanbul, Türkiye, 2004.
23. Senel, M. *Fethiye-M-8 Paftası, 1:100.000 Olcekli Turkiye Jeoloji Haritalari, No:4*; MTA Jeoloji Etutleri Dairesi: Ankara, Türkiye, 1997.
24. Aydin, B.; Yalcin, F.; Ozer, O.; Yalcin, M.G. Regression Analysis and Statistical Examination of Knoop Hardness on Abrasion Resistance in Lyca Beige Marbles. *Filomat* **2020**, *34*, 609–614. [CrossRef]
25. Feng, J.L. Behaviour of rare earth elements and yttrium in ferromanganese concretions, gibbsite spots, and the surrounding terra rossa over dolomite during chemical weathering. *Chemical Geol.* **2010**, *271*, 112–132. [CrossRef]
26. Fedo, C.M.; Nesbitt, H.W.; Young, G.M. Unravelling the Effects of Potassium Metasomatism in Sedimentary Rocks and Paleosols, with Implications for Paleoweathering Conditions and Provenance. *Geology* **1995**, *23*, 921–924. [CrossRef]
27. Bahlburg, H.; Dobrzinski, N. A Review of The Chemical Index of Alteration (CIA) and Its Application To The Study of Neoproterozoic Glacial Deposits and Climate Transitions. *Geol. Soc.* **2011**, *36*, 81–92. [CrossRef]
28. Nesbitt, H.W.; Young, G.M. Early Proterozoic Climates and Plate Motions Inferred from Major Element Chemistry of Lutite. *Nature* **1982**, *299*, 715–717. [CrossRef]
29. Harnois, L. The CIW index: A New Chemical Index of Weathering. *Sediment. Geol.* **1988**, *55*, 319–322. [CrossRef]
30. Price, J.R.; Velbel, M.A. Chemical Weathering Indices Applied to Weathering Profiles Developed on Heterogeneous Felsic Metamorphic Parent Rocks. *Chem. Geol.* **2003**, *202*, 397–416. [CrossRef]
31. Ruxton, B.P. Measures of The Degree of Chemical Weathering of Rocks. *J. Geol.* **1968**, *76*, 518–527. [CrossRef]
32. Aksoy, E.; San, B.T. Geographical information systems (GIS) and Multi-Criteria Decision Analysis (MCDA) integration for sustainable landfill site selection considering dynamic data source. *Bull. Eng. Geol. Environ.* **2019**, *78*, 779–791. [CrossRef]
33. San, B.T.; Ulusar, U.D. An approach for prediction of shoreline with spatial uncertainty mapping (SLiP-SUM). *Int. J. Earth Obs. Geoinf.* **2018**, *73*, 546–554. [CrossRef]
34. Bland, W.; Rolls, D. *Weathering: An Introduction to Scientific Principles*; Arnold: London, UK, 1998.
35. Raiswell, R.W.; Brimblecombe, P.; Dent, D.L.; Liss, P.S. *Environmental Chemistry: The Earth Air–Water Factory*; J. Wiley Sons: London, UK, 1980.
36. Hanilci, N. Geological and Geochemical Evolution of The Bolkardagi Bauxite Deposits, Karaman, Turkey: Transformation from Shale to Bauxite. *J. Geochem. Explor.* **2013**, *133*, 118–137. [CrossRef]
37. Schellmann, W. Eine neue Laterit definition. *Geol. Jahrb. Reihe D* **1982**, *58*, 31–47.
38. *ESRI ArcGIS Desktop: Release 10*; Environmental Systems Research Institute: Redlands, CA, USA, 2011.
39. Temur, S.; Orhan, H.; Deli, A. Geochemistry of The Limestone of Mortas Formation and Related Terra Rossa, Seydisehir, Konya, Turkey. *Geochem. Int.* **2009**, *47*, 67–93. [CrossRef]
40. Yalcin, M.G.; Battaloglu, R. Investigation of Heavy Metals Pollution Along The Nigde-Kayseri Road, Turkey. *Asian J. Chem.* **2007**, *19*, 2257–2264.
41. Yalcin, M.G.; Narin, I.; Soylak, M. Heavy Metal Contents of The Karasu Creek Sediments, Nigde, Turkey. *Environ. Monit. Assess.* **2007**, *128*, 351–357. [CrossRef]
42. Yalcin, M.G.; Tumuklu, A.; Sonmez, M.; Erdag, D.S. Application of Multivariate Statistical Approach to Identify Heavy Metal Sources In Bottom Soil of The Seyhan River (Adana), Turkey. *Environ. Monit. Assess.* **2010**, *164*, 311–322. [CrossRef]
43. Yalcin, M.G.; Simsek, G.; Ocak, S.B.; Yalcin, F.; Kalayci, Y.; Karaman, M.E. Multivariate Statistics and Heavy Metals Contamination in Beach Sediments from The Sakarya Canyon, Turkey. *Asian J. Chem.* **2013**, *25*, 2059. [CrossRef]
44. Ji, H.; Chang, C.; Beckford, H.O.; Song, C.; Blake, R.E. New Perspectives on Lateritic Weathering Process Over Karst Area–Geochemistry and Si-Li Isotopic Evidence. *Catena* **2021**, *198*, 105022. [CrossRef]
45. Yalcin, M.G.; Narin, I.; Soylak, M. Multivariate Analysis of Heavy Metal Contents of Sediments from Gumusler Creek, Nigde, Turkey. *Environ. Geol.* **2008**, *54*, 1155–1163. [CrossRef]
46. Yalcin, M.G.; Aydin, O.; Elhatip, H. Heavy Metal Contents and The Water Quality of Karasu Creek in Nigde, Turkey. *Environ. Monit. Assess.* **2008**, *137*, 169. [CrossRef]
47. Tarinc, O.K.; Ozer, O.; Aydin, B.; Yalcin, M.G. Comparison of physical-mechanical properties of Clova and Lyca marbles in Akcay (Antalya) region by using independent-samples T-test statistics. In Proceedings of the The 2nd Mediterranean International Conference of Pure Applied Mathematics and Related Areas, Paris, France, 28–31 August 2019; pp. 28–31.
48. Yalcin, F.; Ozer, O.; Nyamsari, D.G.; Yalcin, M.G. Statistical Evaluation of The Geochemical Content of Beach Sand Along the Sarisu-Kemer Coastline of Antalya, Turkey. In Proceedings of the AIP Conference Proceedings, Rhodes, Greece, 13–18 September 2018; Volume 2116, p. 100005.
49. Yalcin, M.G.; Coskun, B.; Nyamsari, D.G.; Yalcin, F. Geomedical, Ecological Risk, and Statistical Assessment of Hazardous Elements in Shore Sediments of The Iskenderun Gulf, Eastern Mediterranean, Turkey. *Environ. Earth Sci.* **2019**, *78*, 438. [CrossRef]
50. Ozer, O.; Yalcin, M.G. Correlation of Chemical Contents of Sutlegen (Antalya) Bauxites and Regression Analysis. In Proceedings of the AIP Conference Proceedings, Jodhpur, India, 18–22 December 2020; Volume 2293, p. 180008.
51. Ince, Z.; Atakoglu, O.O.; Yalcin, M.G. Multivariate and Spatial Statistical Analysis of Geochemical Data of Dolomite: The Case of Industrial Raw Materials' Differentiation. *Montes Taurus J. Pure Appl. Math.* **2021**, *3*, 1–21.
52. Battaloglu, R.; Candar, S.; Yalcin, M.G.; Yalcin, F. Component Analysis and Determination of Heavy Metal Accumulation in Euphorbia macroclada Boiss (Nigde, Turkey). *Asian J. Chem.* **2013**, *25*, 8545. [CrossRef]

53. Yalcin, M.G.; Setti, M.; Karakaya, F.; Sacchi, E.; Ilbeyli, N. Geochemical and Mineralogical Characteristics of Beach Sediments Along The Coast Between Alanya and Silifke (Southern Turkey). *Clay Miner.* **2015**, *50*, 233–248. [CrossRef]
54. Yalcin, F.; Kilic, S.; Nyamsari, D.G.; Yalcin, M.G.; Kilic, M. Principal Component Analysis of Integrated Metal Concentrations of Bogacayi Riverbank Sediments in Turkey. *Pol. J. Environ. Stud* **2016**, *25*, 471–485. [CrossRef]
55. Yalcin, M.G.; Ilhan, S. Major and Trace Element Geochemistry of Bauxites of Ayranci, Karaman, Central Bolkardag, Turkey. *Asian J. Chem.* **2016**, *25*, 2893–2904. [CrossRef]
56. Yalcin, F.; Nyamsari, D.G.; Paksu, E.; Yalcin, M.G. Statistical Assessment of Heavy Metal Distribution and Contamination of Beach Sands of Antalya-Turkey: An Approach to The Multivariate Analysis Techniques. *Filomat* **2016**, *30*, 945–952. [CrossRef]
57. Yalcin, M.G.; Cevik, O.; Karaman, M.E. Use of Multivariate Statistics Methods to Determine Grain Size, Heavy Metal Distribution and Origins of Heavy Metals in Mersin Bay (Eastern Mediterranean) Coastal Sediments. *Asian J. Chem.* **2016**, *25*, 2696–2702. [CrossRef]
58. Ozer, O.; Yalcin, F.; Nyamsari, D.G.; Yalcin, M.G. Appraisal of Metal Accumulation in Beach Sand Using Contamination Indices and Multivariate Statistical Analysis. In Proceedings of the 2nd Mediterranean International Conference of Pure Applied Mathematics and Related Areas, Paris, France, 28–31 August 2019; pp. 1–5.
59. Tumuklu, A.; Sunkari, E.D.; Yalcin, F.; Ozer Atakoglu, O. Data Analysis of the Gumusler Dam Lake Reservoir Soils Using Multivariate Statistical Methods (Nigde, Türkiye). *Int. J. Environ. Sci. Technol.* **2023**, *20*, 5391–5404. [CrossRef]
60. Atakoglu, O.O.; Yalcin, F. Evaluation of The Surface Water and Sediment Quality in the Duger Basin (Burdur, Turkey) Using Multivariate Statistical Analyses and Identification of Heavy Metals. *Environ. Monit. Assess.* **2022**, *194*, 484. [CrossRef]
61. Ozer Atakoglu, O.; Yalcin, M.G.; Ozmen, S.F. Determination of Radiological Hazard Parameters and Radioactivity Concentrations in Bauxite Samples: The Case of the Sutlegen Mine Region (Antalya, Turkey). *J. Radioanal. Nucl. Chem.* **2021**, *329*, 701–715. [CrossRef]
62. Atakoglu, O.O.; Yalcin, M.G. Geochemical Characterization of The Sutlegen Bauxite Deposit, SW Antalya. *Min. Miner. Depos.* **2021**, *15*, 108–121. [CrossRef]
63. Kaiser, M.O. Kaiser–Meyer–Olkin Measure for Identity Correlation Matrix. *J. R. Stat. Soc.* **1974**, *52*, 296–298.
64. Yalcin, F. Application of Multivariate Statistic and Pollution Index Techniques to Determine Beach Sand Element Distribution, East of Antalya City. *Filomat* **2020**, *34*, 623–630. [CrossRef]
65. Yalcin, F. Data Analysis of Beach Sands' Chemical Analysis Using Multivariate Statistical Methods and Heavy Metal Distribution Maps: The Case of Moonlight Beach Sands, Kemer, Antalya, Turkey. *Symmetry* **2020**, *12*, 1538. [CrossRef]
66. Leventeli, Y.; Yalcin, F. Data Analysis of Heavy Metal Content in Riverwater: Multivariate Statistical Analysis and Inequality Expressions. *J. Inequalities Appl.* **2021**, *1*, 14. [CrossRef]
67. Sharma, S. *Applied Multivariate Techniques*; John Wiley and Sons Inc.: New York, NY, USA, 1996; 512p.
68. Ozer, O.; Yalcin, F.; Tarinc, O.K.; Yalcin, M.G. Investigation of Suitability of Marbles to Standards With Inequality Expressions and Statistical Approach Using Some Physical and Mechanical Properties. *J. Inequalities Appl.* **2020**, *2020*, 97. [CrossRef]
69. Yalcin, F.; Jonathan, M.P.; Yalcin, M.G.; Ilhan, S.; Leventeli, Y. Investigation of Heavy Metal Content in Beach Sediments on The of Tasucu Bay (Mersin) With Geochemical and Multivariate Statistical Approaches. *J. Eng. Sci. Des.* **2020**, *8*, 1113–1125.
70. Yalcin, F.; Unal, S.; Yalcin, M.G.; Akturk, O.; Ocak, S.B.; Ozmen, S.F. Investigation of The Effect of Hydrothermal Waters on Radionuclide Activity Concentrations in Natural Marble with Multivariate Statistical Analysis. *Symmetry* **2020**, *12*, 1219. [CrossRef]
71. Yalcin, M.G. Cluster Analysis Approach to Identify Metal Sources in Bottom Sediments of Sultan Marsh Canals, Turkey. *Int. J. Environ. Health* **2009**, *3*, 106–125. [CrossRef]
72. Yalcin, M.G.; Nyamsari, D.G.; Ozer Atakoglu, O.; Yalcin, F. Chemical and Statistical Characterization of Beach Sand Sediments: Implication For Natural and Anthropogenic Origin and Paleo-Environment. *Int. J. Environ. Sci. Technol.* **2022**, *19*, 1335–1356. [CrossRef]
73. Yalcin, M.G.; Unal, B. Multivariate Statistical Approach to Identify Heavy Metal Sources in Urban Roadside Soils of Manisa, Turkey. *Asian J. Chem.* **2008**, *20*, 3978–3990.
74. Li, Y.; Zhang, H.; Fu, C.; Tu, C.; Luo, Y.; Christie, P. A red clay layer in soils of the Yellow River Delta: Occurrence, properties and implications for elemental budgets and biogeochemical cycles. *Catena* **2019**, *172*, 469–479. [CrossRef]
75. Egli, M.; Fitze, P.; Mirabella, A. Weathering and evolution of soils formed on granitic, glacial deposits: Results from chronosequences of Swiss alpine environments. *Catena* **2001**, *45*, 19–47. [CrossRef]
76. Huang, F.; Wei, X.; Zhu, T.; Luo, Z.; Cao, J. Insights into Distribution of Soil Available Heavy Metals in Karst Area and Its Influencing Factors in Guilin, Southwest China. *Forests* **2021**, *12*, 609. [CrossRef]

Disclaimer/Publisher's Note: The statements, opinions and data contained in all publications are solely those of the individual author(s) and contributor(s) and not of MDPI and/or the editor(s). MDPI and/or the editor(s) disclaim responsibility for any injury to people or property resulting from any ideas, methods, instructions or products referred to in the content.